Theses and dissertations

1-1-2011

Experimental Investigation Of Nanostructures Generated On Glasses Using A MHz Femtosecond Laser

Dheeraj Vipparty
Ryerson University

EXPERIMENTAL INVESTIGATION

OF

NANOSTRUCTURES GENERATED ON GLASSES USING A

MHz FEMTOSECOND LASER

by

Dheeraj Vipparty

B. Eng, Mechanical Engineering, 2009

Ryerson University

A thesis

presented to Ryerson University

in partial fulfillment of the

requirements for the degree of

Master of Applied Science

in the program of

Aerospace Engineering

Ryerson University

Toronto, Ontario, Canada, 2011

Author's Declaration

I hereby declare that I am the sole author of this thesis.

I authorize Ryerson University to lend this thesis to other institutions or individuals for the purpose of scholarly research.

Dheeraj Vipparty

Department of Aerospace Engineering

Ryerson University

I further authorize Ryerson University to reproduce this thesis by photocopying or by other means, in total or in part, at the request of other institutions or individuals for the purpose of scholarly research.

Dheeraj Vipparty

Department of Aerospace Engineering

Ryerson University

Abstract

EXPERIMENTAL INVESTIGATION OF NANOSTRUCTURES GENERATED ON GLASSES USING A MHZ FEMTOSECOND LASER

Master of Applied Science, 2011

Dheeraj Vipparty

Aerospace Engineering

Ryerson University

This dissertation reports the synthesis of unique SiO_2 based nanostructures by exposing glass samples to MHz repletion rate femtosecond laser irradiation. A three-dimensional fibrous nanoparticle agglomerate network was observed on soda-lime glass (73% SiO_2 + other compounds) when exposed to femtosecond laser irradiation at 8.4 MHz and 12.6 MHz repetition rate and 0.5 ms dwell time, in air. By irradiating silica glass (96% SiO_2 + trace elements) sample under ambient conditions with femtosecond pluses at 12.6 MHz and dwell time in excess of 3.0 ms; long continuous nanofibers of extremely high aspect ratio (certain fibers up to 100000:1) were obtained. The mechanisms that promote such nanostructures with distinct morphologies have been explored. A deeper insight into the fundamentals of femtosecond laser interaction with dielectrics led to the understanding that variations in bandgap alters ablation dynamics and dictates the response of glass to femtosecond laser irradiation, ultimately resulting in the formation of structures with dissimilar morphology on silica and soda-lime glass.

Acknowledgements

It is a pleasure to thank those who made this thesis possible. I owe my deepest gratitude to my supervisors Dr. Bo Tan and Dr. Krishnan Venkatakrishnan for their guidance, stimulating suggestions, and support over the past two years. Constructive criticism from both my supervisors has helped overcome the difficulties I faced during my research and in the development of this thesis.

I would like to thank Dr. Jeffrey Yokota, Director of Aerospace Engineering Graduate program, all the faculty members, technical officers and administrative staff members for their kind support and cooperation during my stay at Ryerson University.

I am thankful to my fellow lab-mates: Hamsapriya Selvaraj and Champika Samarasekera for providing a comfortable and co-operative working environment. Their valuable help is appreciated a lot. I would like to thank my friends: Rizwan Ikramuddeen, Charan Thej Tula, Golam Morshed, Palneet Waraich, and Nikunj Patel for all their support. I would also like to thank my cousin, Sridhar Lam, for his valuable advice and suggestions.

I would like to thank my parents, Dr. Surya Kumar Vipparty and Dr. Jhancy Nirmala Nalli for their unconditional love, never-ending support and words of encouragement. Finally, my special gratitude is always due to my brother, Manoj Vipparty, for his loving support during the difficult times.

Table of Contents

Chapter 1

Introduction

Chapter 2

Ultrashort Pulse Laser Interaction with dielectrics

Chapter 6

Conclusion and Future work

List of Tables

List of Figures

List of Appendices

Nomenclature

Ns	Nanosecond (10^{-9}s)
ps	Picosecond (10^{-12}s)
fs	Femtosecond (10^{-15}s)
µs	Microsecond (10^{-6}s)
Ms	Millisecond (10^{-3} s)
µm	Micrometer (10^{-6} m)
cm	Centimeter (10^{-2}m)
In	Inches
MHz	Megahertz (10^6 Hz)
kHz	Kilohertz (10^3 Hz)
nm	Nanometer (10^{-9} m)
Mm	Micrometer (10^{-3} m)
W	Watt
GW	Gigawatt (10^9 s)
eV	Electron Volt
K	Kelvin
Deg, º	Degree Celsius
J	Joule
µJ	Micro-Joule (10^{-6} J)
2D	2 Dimensional
3D	3 Dimensional
UV	Ultra violet
T_e	Electron temperature
T_i	Lattice temperature
I(t)	Laser intensity at time t
α	Absorption coefficient
k_e	Electron thermal conductivity
I_0	Intensity

t	Time
τ_L	Laser pulsewidth
τ_e	Electron cooling time
τ_i	Lattice heating time
F_a	Ablation fluence
F_{th}, $ø_{th}$	Threshold fluence
l_s	Skin depth
D	Heat diffusion coefficient
E	Energy deposited inside target per unit mass
ρ	Density
P	Average power of the laser pulse
R	Reflection coefficient
r	Reciprocal of pulse interval
I_{th}	Threshold intensity
F	Laser fluence
T_0	Temperature at time t = 0
T_i	Initial temperature
ω_0	Radius of the laser focal spot
λ_0	Wavelength of the laser beam

Chapter 1
Introduction

1.1   Nanotechnology and potential aerospace applications

In aerospace and aeronautics industries, the aircraft ownership costs and operating costs are quite high, therefore there is a need for novel and efficient materials that can reduce the expenses either by reducing weight (thereby decreasing fuel consumption) or by lessening Maintenance, Repair and Operation (MRO). Nanotechnology is capable of developing new materials that can meet this requirement.

Nano-composites are materials comprised of nanotubes, nanofibers, nanoparticles, fullerines in polymer, carbon, ceramic, or metal marices. Such composite material can significantly enhance thermal conductivity, directional anisotropy, radiation absortption, and structural reinforcement [1]. Therefore, the influence of these materials (nano-composites) spreads across virtually all aircraft components and systems, extending from airframes to propulsion systems, and from windows or interiors to electrical and electronic systems [1].

The primary application of nanomaterials that contribute to aircraft construction is airframe structure. However, these materials also provide applications to the interior to a minor degree[1]:

- The use of nanomaterials results in weight reduction and therfore decrease fuel consumption because of high strength-to-weight ratio

- Stronger material of the same weight increases impact resistance of aircraft skin material, which allows for the aircraft to perform efficiently even in extreamly harsh conditions

- Aircraft safety can be increased through the use of new materials in the interior. For instance, the development of light bullet proof materials for sensitive parts, e.g. the cockpit door

- An important aspect for the interior of an aircraft is the need for fire retardant materials. The goal is to meet the stringent specificatios for the interior material with a cheaper nano-material than the costly specilized polymers currently used

- Superior air quality can be mainted in the cabin by using filtration systems that use nanofibers which block/trap extreamly fine particles

- Coating metal with nanomaterials (nanoparticles or nanofibers) cretes a protective layer and corrosion can be decreased

- By coating aircaft turbine blades with nanomaterials, the metal blades can run at hotter temperatures

These applications of nanotechnology can be fully realized only with a continued fundamental research in the development of unique and novel nanostructures.

1.2 Nanostructures

Structures that have at least one dimension between 1 and 100 nm are termed *nanostructures* [2]. These structures have gained much attention in the field of research and development during the recent years due to their unique properties which are primarily governed by their high surface area to volume ratio. In the nanoscale regime, materials exhibit physical properties distinctively different from their bulk counterpart [3]. Size-dependent properties are the reason that nanoscale structures such as: nanofibers and nanoparticles are being used in modern science and technology for various applications.

1.3 Nanofibers

Nanofibers are simple one-dimensional nanostructures. Silica glass based nanofibers possess exceptional mechanical and tensile properties [4]. Therefore, nanofibers have been employed for a wide range of applications such as filter media [5, 6], tissue engineering [7], reinforcement in composites and micro/nano-electro-mechanical systems (M/NEMS) [8]. The sub-wavelength nanofibers generated from glass can be utilized as waveguides for optical communication, and as sensors [6]. There have been several techniques reported to produce nanofibers such as: drawing, electrospinning, ball milling, and pulsed laser ablation. These techniques have been elaborated in the following section.

1.4   Nanofiber Fabrication Methods

1.4.1 Taper Drawing

Tong *et al.* reported a two-step drawing process for fabricating long uniform silica nanowires with dimensions in nanometers using a flame-heated drawing method [9]. The primary step involves using flame-brushing technique to reduce the diameter of a silica fiber from few millimeters to micrometers. Flame-brushing procedure utilizes a small flame which moves beneath a stretched optical fiber (Figure 1–1). The fiber diameter is lowered by accurately controlling (via a computer) the flame motion and the stages attached to the either ends of the stretched fiber [4].
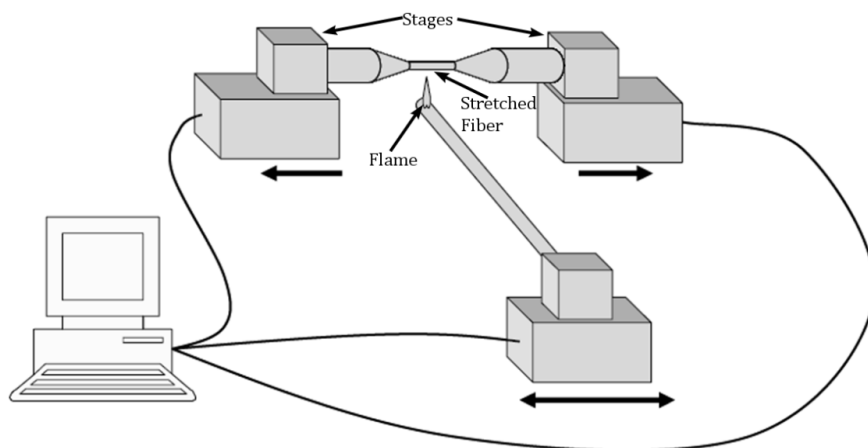
Figure 1–1: Flame-brushing technique. The fiber diameter is controlled by precisely adjusting the flame and stage movement [4]

In the secondary step, the micron fiber diameter is further reduced to nanometer level, and this step requires even temperature distribution. Hence, a sapphire fiber taper with a tip diameter of about 80 µm is used to absorb thermal

4

energy from the flame and evenly distribute the temperature to a small confined volume (Figure 1–2b). Subsequently, one end of the micrometer fiber is placed horizontally over the sapphire tip and the flame heat is increased until the temperature of the tip is just above drawing temperature (about 1726.85 °C). The sapphire tip is then rotated around its axis of symmetry to allow for the silica fiber to coil around the tip (Figure 1–2a). Afterwards, the fiber is drawn/pulled in a direction perpendicular to the axis of the sapphire tip (Figure 1–2c) at speeds from 1 mm/s to 10 mm/s to generate fibers of varying diameter in nanometer range [10, 11]

.
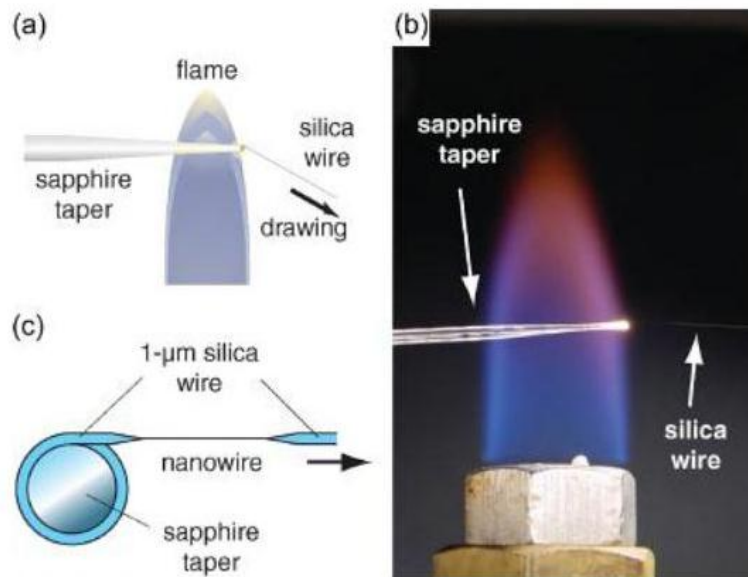
Figure 1–2: Two-step taper drawing of silica nanofibers. a) The silica fiber coil and sapphire tip being heated to the required temperature. b) Close-up of second-step. c) The process that generates nanofibers. (From Ref. [11])

5

The two-step drawing technique can produce single strand of aligned nanowires with diameters ranging from 50 to 1100 nm and lengths up to tens of millimeters, with minimum irregularities along the surface.

The second step of the taper drawing process can be further modified by applying self-modulated drawing force to fabricate fibers with diameters less than 100 nm and with intrinsic surface diameters [9]. In this self-modulation phase, an elastic bend is introduced around the silica fiber taper area by holding the fiber parallel to the sapphire taper while ensuring the connection between the silica fiber and the sapphire taper is not severed [11]. The tautening of fiber into 90° elastic bend generates a tensile force that can be implemented for self-modulation as shown in Figure 1–3a. During the initial stage when thick fibers are drawn with relatively large force, the sharpest bend appears at the thicker part of the silica fiber taper (Figure 1–3c). A continued elongation of the fiber reduces the diameter. The bend relaxes and the bending center progressively shifts toward the thinner end of the taper. Subsequently, this results in smaller forces drawing uniform fibers with smaller diameter. The self-modulation phenomenon compensates unpredictable undulations such as, temperature fluctuations by moving the bending center and smoothens out any abrupt changes in diameter [9, 11].

The silica nanofiber produced from self-modulated taper-drawing have diameters as small as 20 nm [9].
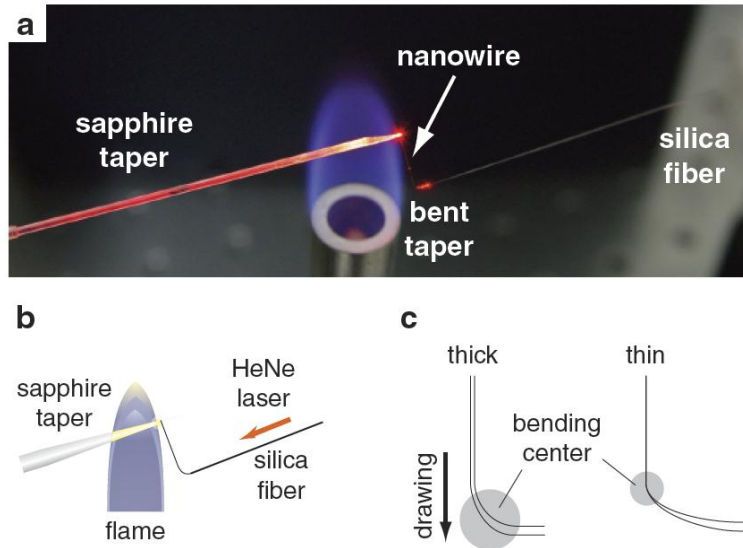
Figure 1–3: Taper drawing of silica nanofiber via Self-modulation. a) Close-up of nanowire drawing with 90° bend illuminated by laser. b) Schematic of the setup. c) As the fiber is drawn, self-modulation shifts the center. (From Ref. [11]**)**

1.4.2 Electrospinning

The process of spinning fibers with the help of electrostatic forces is known as electrospinning [12]. Electrospinning process involves electrically charging the polymer solution held in a pipette. The applied electric field and electrostatic interactions generate a stretching force that causes the polymer jet to erupt out of the orifice of the cone at a high acceleration. The subsequent evaporation and solidification of fiber jet results in dry fibers deposited on grounded collector [13].

The basic setup of electrospinning is shown in Figure 1–4 and it consists of three important components: a high voltage power supply, a spinneret (metallic needle), and a collector (a grounded conductor). On application of high voltage, the drop of solution at the nozzle of the spinneret undergoes electrification which causes the induced charges to spread evenly across the surface. Consequently, two major

electrostatic forces: the electrostatic repulsion between the surface charges and the coulomb forces of the external field are generated which act on the drop of solution. Under the influence of these electrostatic forces the liquid drop is transformed into the Taylor cone (Figure 1–4, Inset). As the magnitude of electric field exceeds the threshold value; the electrostatic forces overcome the surface tension of the solution and drive the polymer solution through the opening of Taylor cone. The transformation from electrified jet to long and thin thread occurs as the jet undergoes a whipping and stretching process. The continuous elongation of fiber and evaporation of solvent greatly assists the reduction of fiber diameter from hundreds of micro meter to tens of nanometers. The grounded collector located under the spinneret attracts the fibers and are deposited in a random orientation [14].
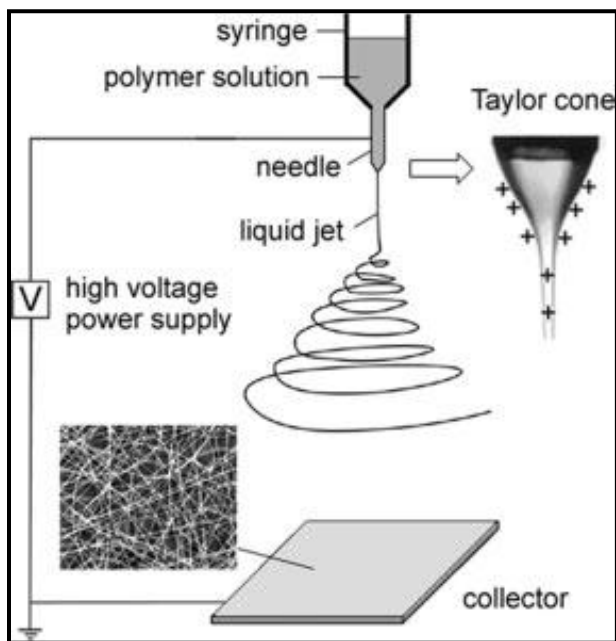
Figure 1–4: Schematic of various components in electrospinning setup. Inset - Taylor Cone (From Ref. [14])

In a study conducted by Choi *et al.,* silica nanofibers were obtained only by combining electrospinning and a sol-gel method. The acquired nanofibers were randomly oriented with diameters ranging from less than 200 nm to more than 1000 nm [15].

1.4.3 Carbothermal reduction synthesis

Wu *et al.* demonstrated a carbothermal reduction process than can fabricate a fiber bunch with individual fibers having diameters in nanometer range [16]. The process involves ball milling of the mixtures of SiO_2, $Fe(NO_3)_3.9H_2O$ and active carbons, for 20 hours in ethanol media. The mixture is pressed into circular pellets under 10 MPa pressure and calcined (heating a substrate to high temperature but below the melting or fusing point) at 1350 ºC for another 3 hours in flowing argon. White power deposited on the pellet surface was observed. TEM (Transmission Electron Microscope) imaging of this powder revealed nanofiber with diameters ranging from 60 to 110 nm with lengths up to 5 μm.

1.4.4 Pulsed laser ablation

Recent publications on pulsed laser ablation of dielectric-sample state that nanosecond [17] and microsecond lasers [18] are capable of producing fibers with diameters in nanometer and micrometer respectively. Nanosecond and microsecond lasers can only produce nanofibers in small quantities and the orientation of the obtained fibers is random in nature (Figure 1–5). Furthermore, there has not been

much research performed to study nanofiber fabrication on substrate surface, hence limited the literature availabile for a review.

Tokarev *et.al* observed nanofibers with a radius of 150-200 nm (Figure 1–5) during ablation of a ploymethyl methacrylate (PMMA) target in air by a single pulse with pulse duration $\tau = 30$ nm [17].
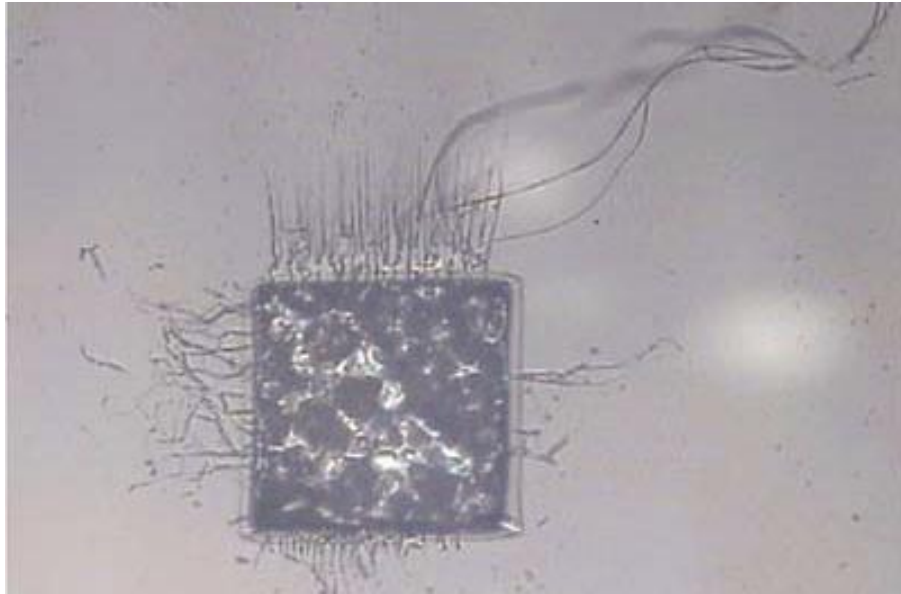
Figure 1–5: Nanosecond laser ablation of PMMA with a single pulse with fluence 5.2 J/cm² resulting in nanofibers (From Ref. [17]).

Silica fibers with 3 μm diameter and lengths ranging from 100 μm to 1 mm (Figure 1–6) were produced by Markillie *et.al* using microsecond laser system. Silica glass samples were exposed to laser irradiation with pulse duration varying in 30-100 μs regime [18].
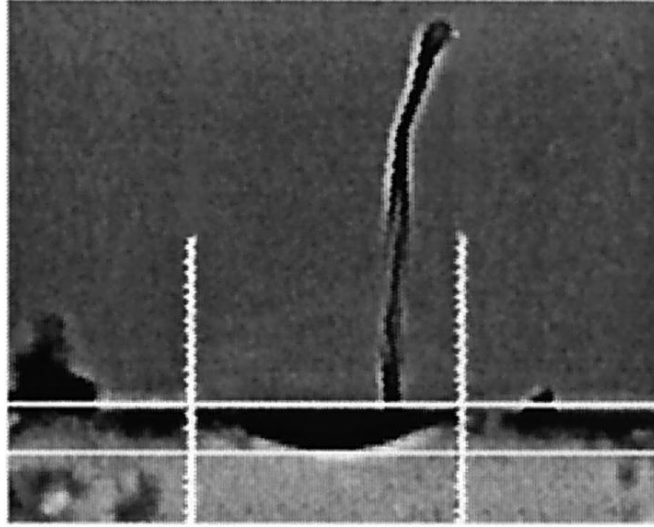
Figure 1–6: Micro fiber generated on silica surface after exposing to 20 µs pulse (From Ref. [18]).

1.4.5 Comparison of nanofiber fabrication techniques

Each of the aforementioned techniques has its advantages and drawbacks. A comparison of these methods is summarized in Table 1-1. For the fabrication of glass nanofibers, drawing is the most attractive method due to its simplicity. However, this process is quite ineffective in producing fibers in large scale, because of its limited capability to fabricate just one individual fiber at a time. Pulsed laser ablation is the only method among the fabricating techniques that can be employed to fabricate fibers from a bulk substrate, but thus far only microfibers of silica and nanofibers of polymers have been reported.

Table 1-1: Summary of nanofiber fabrication techniques

Process		Diameter	Length	Advantages	Disadvantages
Drawing		50-1100 nm	tens of millimeters	Minimum equipment requirement. Excellent diameter uniformity and intrinsic surface smoothness.	The process calls for a high degree precision and is susceptible to any minor fluctuations which can create abrupt taper or breakage of the wire
Electrospinning		200-1000 nm	hundreds of microns	Long, continuous nanofibers can be produced	Jet instability and mostly limited to polymers. This process has to be used in conjunction with sol-gel process to produce silica nanofibers
Carbothermal reduction synthesis		60-110 nm	~5 μm	High volume production	Exhibits a certain degree of complexity in sample preparation. Highly susceptible to contamination. The proposed procedure takes up a considerable amount of time
Pulsed Laser ablation	**Microsecond**	3 μm	100 μm to 1 mm	Single-step process. Requires virtually no sample preparation. Extremely short processing time	Limited control over dimensions of the generated fibers
	Nanosecond	150-200 nm	up to 1 mm		

1.5   Nanoparticles

Nanoparticles are defined as solid particulates or solid particles with dimension less than 100 nm. As a particle gets smaller, there is a gradual increase in the surface area to volume ratio and this leads to an increasing dominance of surface atoms behavior of a particle over that of those in the interior of the particle. Thus, an increase in surface area to volume ratio affects the properties of the particle in isolation and its interaction with other materials. High surface area of nanoparticles allows for a large number of interactions among the intermixed materials in nanocomposites, thereby, improving properties such as strength and/or chemical resistance and/or heat resistance. Furthermore, as the dimensions of nanoparticles are below the critical wavelength of light; nanoparticles are transparent. This characteristic has applications in packing, cosmetics and coating.

There is a wide variety of approaches for producing nanoparticles, but only the techniques employed for the synthesis of silica based nanoparticles have been outlined.

1.6   Fabrication of silica nanoparticles

1.6.1 Vapor condensation

In this method, the vapor phase precursors are brought into a hot-wall reactor that favor nucleation of particles in the vapor phase. The subsequent rapid condensation

process produces nanoparticles [19]. The precursors can be solid, liquid or gas at ambient conditions, but delivered to the reactor as a vapor (Figure 1–7).
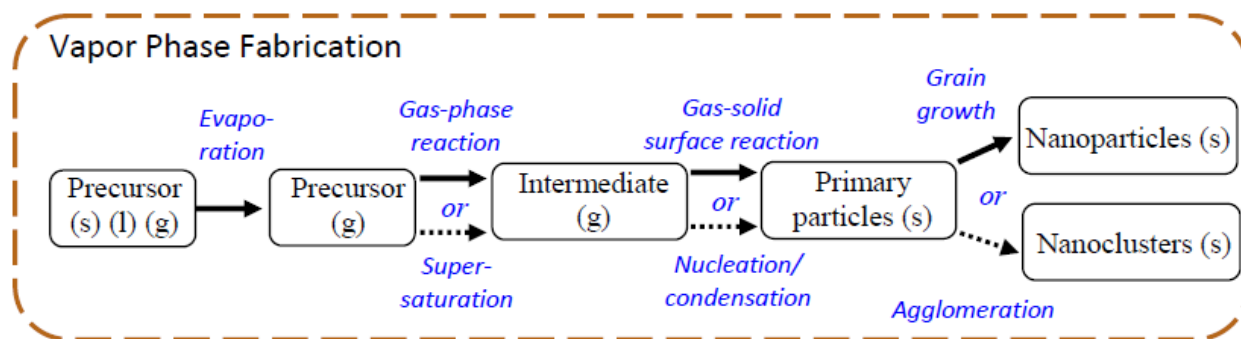
Figure 1–7: Nanoparticle fabrication process [19].

Yu *et.al* reported the synthesis of silica (SiO_2) coated γ-Fe_2O_3 nanocomposite particles by chemical vapor condensation (CVC) process [20]. The experimental procedure (Figure 1–8) involved the use of iron (III) acetylacetonate and tetraethylorthosilicate (TEOS) as precursors. The precursors were delivered to the evaporator via a micro pump. The precursor vapor was then transported into the reactor by helium carrier gas. Simultaneously, the reaction gas (oxygen) was fed into the reactor. The processing temperature was kept at 1000 ºC and pressure 40 mbar. The obtained particles were sampled in the collecting chamber at room temperature, and the obtained particles possessed diameters ranging from 20 to 30 nm.
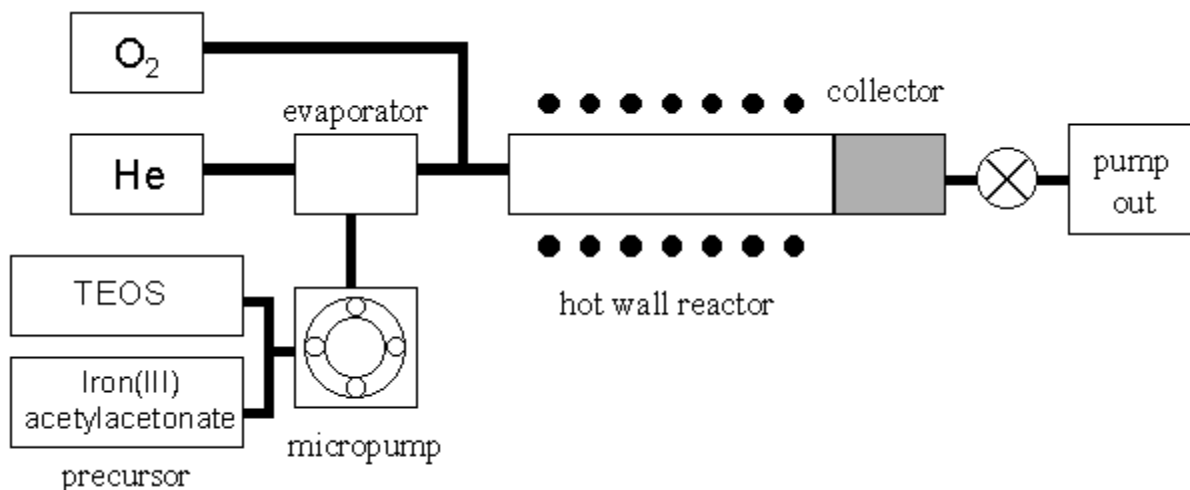
Figure 1–8: Schematic of CVC process [20].

The main advantage of this method is low contamination levels. By varying parameters such as temperature, gas environment and evaporation rate, the final particle size can be controlled.

1.6.2 Chemical synthesis

This process consists growing of nanoparticles in a liquid medium composed of various reactants. This is typified by the sol-gel approach and applied to create nanoparticles.

Sol-gel process is a wet-chemical synthesis approach that generates nanoparticles by gelation, precipitation, and hydrothermal treatment [21].

Zawrah *et.al* reported a method for preparing amorphous silica nanoparticles by sol-gel techniques with sodium silica as a precursor [22]. The preparation of silica nanoparticles involves production of solid silica gel by drop-wise addition of diluted sodium silicate of 28 ml of 2.5% HCL with stirring at 250 rpm at 60 $^{\circ}$C until

15

a cloudy viscous gel was formed. A volume of 10 mL sodium silicate was thoroughly washed with distilled water until free from Cl^- ions. A white precipitate indicates the presence of the ions. The test was repeated until no white precipitate was formed on addition of silver nitrate. The product was placed in oven at 100 ºC for more than 24 hours, and calcined in air at 1000 ºC for 1 hour. The obtained precipitate is composed of nanoparticles.

Chemical synthesis is the most widely used technique to produce nanoparticles because the approach is generally high-volume and low-cost. But, this process is susceptible to contamination from the precursor chemical.

1.6.3 Flame spray pyrolysis

Flame spray pyrolysis is a fabrication process in which a precursor(s), dissolved in a solvent, is sprayed with a carrier gas into a flame zone where the droplets are combusted, and the precursor(s) are converted into nano-sized particles.

Mueller *et.al* employed the flame spray pyrolysis method to generate silica nanoparticles at high production rates (up to 1.1 kg/h) [23].

The experimental setup of the spray pyrolysis plant is shown in Figure 1–9. The process begins by mixing silica precursor, hexamethyldisiloxane (HMDSO) and fuel (ethanol). A 1 liter precision syringe pump is used for feeding precursor solution. By feeding fuel with an additional syringe pump and with subsequent buring, the nozzle is heated for 10 mins.

Finally, the particles are collected on the outside surface of the baghouse filters by an air suction ventilator.
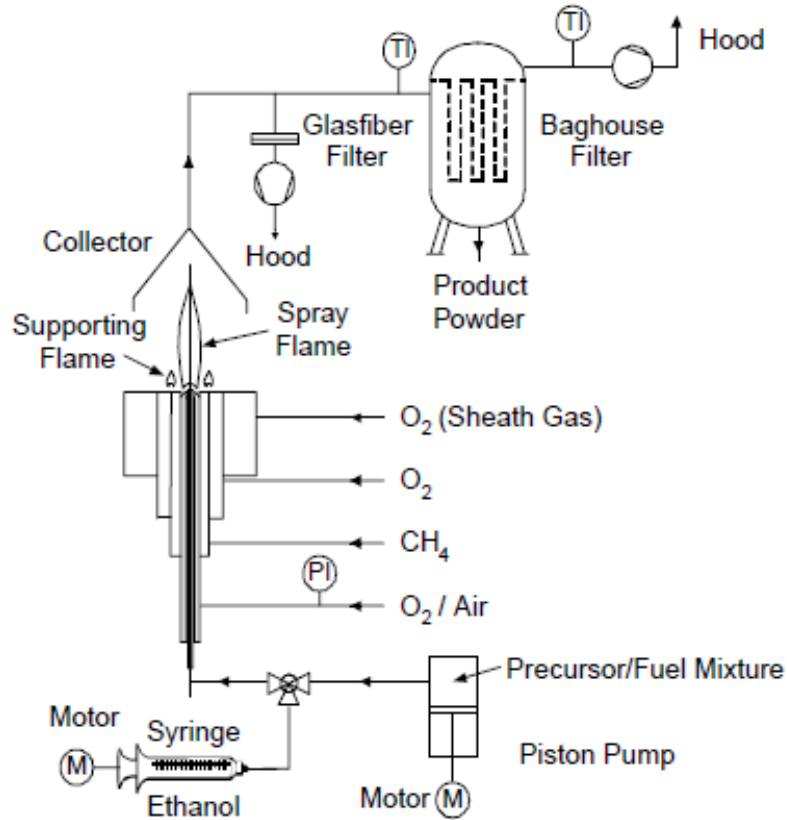
Figure 1–9: Experimental setup for fumed silica nanoparticle synthesis [23]

Flame spray pyrolysis is a rapid production method that can be employed for a wide variety of precursors and has high production rates. But, the process requires extremely precise control over flo-rates of fluids involved and the pressures within the system.

1.6.4 Pulsed laser ablation

Gonzalez *et.al* generated glass particles by ablating series of standard silica glass materials. A femtosecond laser system capable of producing 150 fs laser pulses with fluence 50 J/cm^2 was used [24].

Figure 1–10 shows the SEM (Scanning Electron Microscope) images of the mass collected from femtosecond laser ablation. Agglomerates of nanoparticles were observed in the mass.
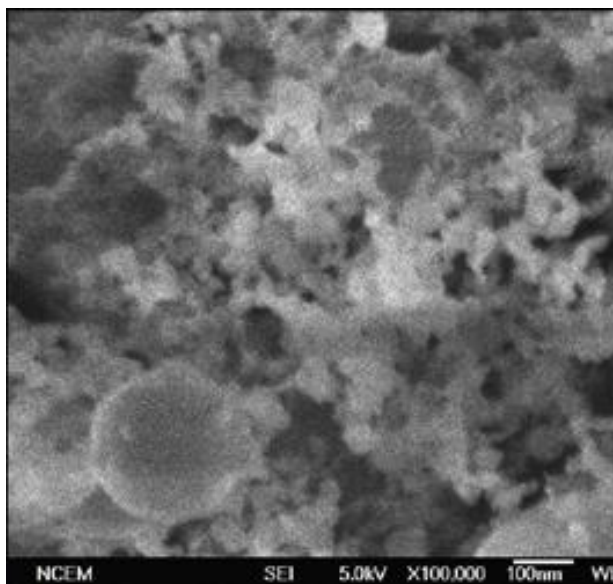
Figure 1–10: SEM image of silica nanoparticles [24]

Glass samples possess low absorptive; therefore the energy absorbed by the glass samples during the interaction is smaller. Although pulsed laser ablation is straightforward nanoparticles fabrication technique compared to other methods, not many pulsed laser systems are capable of delivering the required amount of power

to ablate the sample. Hence, research pertaining to nanostructure synthesis on transparent glass is inadequate.

A comparison of aforementioned nanoparticle fabrication techniques is given in Table 1-2.

Table 1-2: Advantages and disadvantages of nanoparticle fabrication techniques

Process	Advantages	Disadvantages
Vapor condensation	Low contamination levels	Multi-step process
Chemical sythesis	Generally low cost and high throughput	Susceptible to contamination. The procedure takes up considerable amount of time (~ 25 hrs)
Flame spray pyrolysis	High production rates (1.1 kg/h).	Requires extremely precise control over flo-rates of fluids involved and corresponding pressures within the system. Intricate experimental setup
Pulsed Laser ablation	Single-step process. Requires virtually no sample preparation	Limited control over dimensions of the generated nanoparticles

1.7 SiO$_x$ (x = 1-2) nanostructures of varying configurations

Aside nanoparticles and nanofibers, silica based nanostructures of other morphology have been produced by several techniques. Recently, Sauling-Wenger *et.al* reported the one-pot synthesis of amorphous silicon dioxide nanowires and helical self-assembled nanostructures (Figure 1–11a). The fabrication method

involves direct thermal treatment of commercial silicon powder under nitrogen gas flow along with a piece of graphite [25]. Zhu *et.al* have shown the formation of radial flower-like silica structures (Figure 1–11b) (SiO_x, x=1-2) produced by pyrolysis of CO over a mixture of SiC and cobalt powder [26]. Gole *et.al* modified the high temperature synthesis technique proposed by Lee *et.al* and generated virtually defect free SiO_2 sheathed crystalline silicon nanowires and silica (SiO_2) nanospheres which can be agglomerated to wire-like configurations (Figure 1–11c) impregnated with crystalline silicon nanospheres [27].
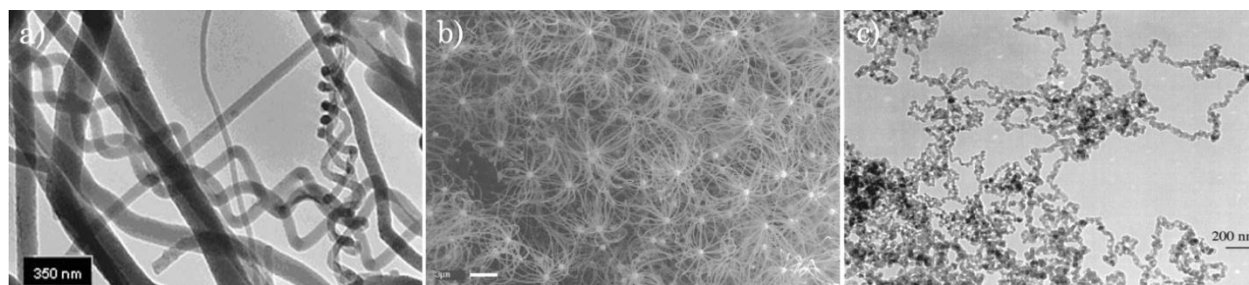
Figure 1–11: Nanostructures of varying morphology. a) Helical nanowires [25]; b) flower-like silica structure [26]; c) agglomerated nanospheres [27].

The production of such novel structures with dimensions in nanoscale regime may exhibit unique physical and mechanical properties and can be explored for various applications. For example, structures of such morphology can be employed in the production of nanocomposites with better efficiency than the existing composites. These structures also can serve as mechanical supports and tissue scaffolds for cell proliferation.

1.8   Research Objectives

The fundamental requirement for nanotechnology to thrive is to fabricate novel 1-D and 3-D nanostructures. Silica based nanostructures have gained much attention because of their potential application in mesoscopic research which deals with development of nanodevices, and nanocomposites [28].

In this context, nanostructures generated by a **femtosecond laser system** were investigated by studying the following.

- Synthesis of nanostructures on various types of glass (SiO_2 based) using MHz repetition rate femtosecond laser and investigate the mechanisms that promote nanostructure on glass samples

- Study the fundamentals of (MHz) femtosecond laser ablation of dielectric material

- The effect of Megahertz (MHz) repetition rate of femtosecond laser on ablation dynamics

1.9   Thesis Outline

Chapter 2 is prepared to provide the details pertaining to Ultrashort Pulse Laser interaction with dielectrics, which includes: (a) nonlinear laser energy deposition (process) into the material, (b) ablation mechanism (material removal), and (c) multiple pulse incubation and thermal effects. A literature review of femtosecond laser interaction with transparent dielectrics has also been given in this chapter. Chapter 3 outlines the experimental procedures. Chapter 4 presents the results of

femtosecond laser ablation – nanofiber production on silica glass surface. The mechanisms that generate these fibers have been discussed. In Chapter 5 the comparison of various nanostructures generated on SiO_2 based glasses (silica and soda-lime) have been detailed. The differences in morphology have been explained by taking into account the variations in bandgap energies. Finally, Chapter 6 provides the conclusions based on the study and gives some ideas for future work in the field of nanofabrication.

Chapter 2

Ultrashort Pulse Laser Interaction with dielectrics

2.1   Introduction

Laser ablation is the process of removing material by exposing the solid surface to laser irradiation. The two kinds of laser employed for material processing are continuous wave (CW) laser and pulsed laser. CW lasers are generally used for macroscopic processing. Ultrafast pulsed lasers have immense potential for precise and efficient material processing at nanoscale due to their tremendously high intensity, ultrashort pulse duration (laser interaction time with target) and non-contact nature of processing. With pulsed lasers, the intensity of peak instantaneous power can be drastically increased by decreasing the pulse duration [29]. Thus, ultrashort pulsed lasers (femtosecond and picosecond lasers) are capable of achieving very high peak laser intensity with low pulse energies. For example, a laser pulse with a pulse-duration of 100 fs and pulse energy of only one-third of 1 mJ when focused to a spot diameter 20 μm yields a peak intensity of 10^{15} W/cm^2. For a 10 nanosecond laser pulse to acquire the same intensity, pulse energy of 100 J would be required [30]. At such enormous intensities, nonlinear processes become profound and evoke efficient absorption in materials including transparent dielectrics. Due to the extreme short nature of ultrafast pulse, the pulse is completed earlier than hydrodynamic expansion and material removal. Consequently, the energy deposition happens at solid-state densities. Since femtosecond lasers transfer energy into the target material in a very short interval

of time, thermal energy is concentrated in and around the focal region shunning thermal diffusion [31]. As the ablation process can be temporally separated into energy deposition and material removal, the ejected material does not interact with the laser pulse. The amalgamated effect of femtosecond laser ablation is an improvement in the localization of energy deposition with reduced heat and shock affected zone leading to precise ablated features.

2.2   Dynamics of ultrafast pulsed laser ablation

The dynamics of the ablation process can be divided roughly into two stages: the photon energy absorption, mainly through free electron generation and heating, and the redistribution of the absorbed energy to the lattice, leading to material removal [32].

2.2.1 Energy absorption

The first step in laser ablation is the absorption of laser energy by the target material. In dielectrics, the energy is absorbed to excite electrons from the valance to the conduction band. The interband excitation can only occur if the incident photon energy exceeds the bandgap energy of the dielectric material. But for dielectrics the bandgap is larger than the photon energy. Therefore, nonlinear processes such as: multiphoton transitions and avalanche ionization are necessary to promote the initial creation of the free-carriers [33-36].

The avalanche ionization process is illustrated in Figure 2–1. At low intensities, the bound electrons do not absorb the laser energy. However, in any real materials some free or conduction electrons exist, and they act as seed electrons for

avalanche ionization. Seed electrons can occur due to metallic impurities, thermal or linear optical ionization of shallow energy levels of inclusions [30]. A free electron can be excited to the conduction band by absorbing several laser photons. An electron with such high energy can ionize another electron form the valence band, resulting in two excited electrons. This is known as inverse Bremsstrahlung process or joule heating process. An accelerated seed electron collides with a bound electron with enough acceleration that its kinetic energy surpasses the ionization potential of the bound electron. During this collision nearly all of the free electron energy is transferred to the bound electron. Consequently, two free electrons with low kinetic energies are created (Figure 2–1). This is termed as impact ionization. This process will repeat itself causing an avalanche and the density of free-electron increases exponentially. As the avalanche process furthers ionizes the bound electrons, plasma with a "critical density" is created, and this initiates the breakdown of transparent material. Subsequently the dielectric material becomes more absorbing (the absorption, initially is negligible due to the very low free-electron density). Close to the ablation threshold the free-electron density in the conduction of the dielectrics is in the order of 10^{21} cm^{-3} [37].
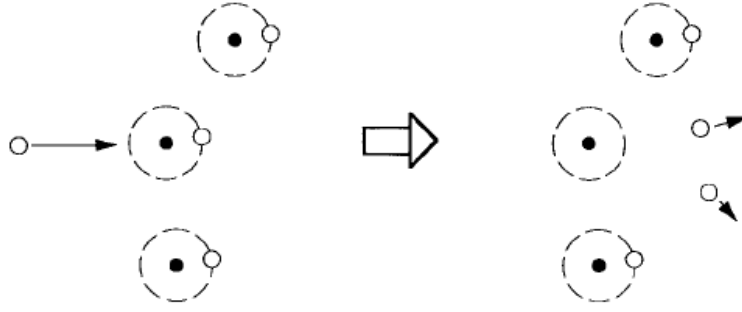
Figure 2–1: Schematic of electron avalanche by collision impact ionization

With high laser field strength ($> 10^9$ W/cm²) of femtosecond laser pulses, bound electrons can be ionized during laser-matter interaction via multiphoton absorption. The schematic of this process is shown in Figure 2–2. By simultaneous absorption of m photons, a bound electron can be excited from ground state (valence band) to free energy state (conduction band) such that $mh\nu \geq U_1$, where $h\nu$ is the energy of the photon, and U_1 is the ionization potential or bandgap. This is termed as multiphoton ionization. Since multiphoton ionization is m th order process, it is significant only at very high laser field strength Therefore, for longer pulse-durations ($> 10^{-9}$ S) with lower laser field strength the contribution of multiphoton ionization is minimal, and the breakdown in longer pulses is dominated by avalanche ionization. However, at ultrashort pulse durations (femtosecond, picosecond), multiphoton ionization plays an important role: it determines the breakdown threshold behavior.

The avalanche and multiphoton ionization nonlinear processes occur simultaneous during the laser-material interaction; hence it is difficult to assess the contribution of each channel.
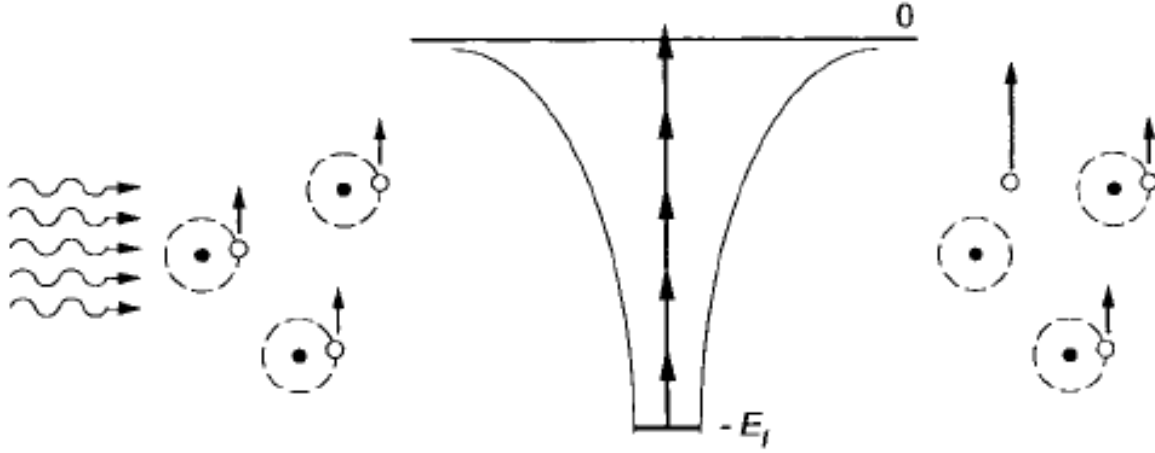
Figure 2–2: The multiphoton ionization process

2.2.2 Energy transfer

The free electron density (in the conduction band), upon reaching a critical value triggers the material breakdown process. The free electrons attain thermal equilibrium, via carrier-carrier scattering. And, immediately undergo rapid electron-phonon relaxation responsible for energy transfer to the lattice in the order of few picoseconds [38]. The thermal energy possessed by electrons is rapidly dissipated via heat conduction, and the electron-atom interaction steadily increases the temperature of the atoms in the lattice. After several picoseconds, a thermal equilibrium is attained between atoms and electrons [39]. The lattice, upon reaching a temperature of certain degree, undergoes volumetric phase change accompanied by material decomposition. The above explained mechanism is termed as "thermal" ablation due to the fact that it is caused by intense temperature of the material. The existence of Coulomb forces between electron cloud and atoms induces

27

repulsive forces between the two subsystems and invokes the disintegration of material which results in "non-thermal" ablation process (Coulomb explosion) [40]. Both Thermal and non-thermal ablations contribute to the formation and expansion of plasma during femtosecond laser irradiation.

2.2.3 Succeeding processes

Hydrodynamic expansion of the ablated material starts few 100 ps after the initial excitation. Theoretical investigations have identified several ablation mechanisms such as: spallation, explosive boiling, vaporization, and melt expulsion [17, 41, 42]. The initiation of a specific expansion mode depends on the amount of energy absorbed and composition of the material.

If the laser fluence (energy/area) is just above the damage threshold (fluence at which damage to the target is induced), the fast energy deposition of short-pulse laser leads to steep temperature rise in the focused area and generates tensile stresses sufficiently high at the irradiated spot to cause mechanical fracture of brittle material or promote cavitation and fragmentation in a metastable liquid. This type of material removal caused by laser-induced stress is called as front-surface spallation [43].

At a higher fluence, beyond the damage threshold, the irradiated surface can overheat beyond the limit of its thermodynamic stability, leading to an explosive decomposition of the overheated material into a mixture of vapor and liquid droplets. This process is termed as phase explosion or explosive boiling [43]. The rapid boiling process is due to the homogeneous nucleation of superheated liquid

near its critical state. The high-irradiance of an ultrashort pulse rapidly melts the surface, and the molten material is heated beyond its thermodynamic boiling temperature. The subsequent bubble formation can be attributed to the density fluctuations in the superheated molten pool. Ultimately, enough pressure is exerted by the rapidly expanding bubble within the volume, leading to the ejection of mass. Phase explosion is believed to be the primary mechanism in femtosecond ablation, when the laser intensity is below the threshold of plasma formation [44].

At fluence above the threshold of plasma formation, a layer of material surface can be atomized via vaporization process. The term vaporization does not refer to evaporation from the surface layer; instead vaporization describes complete dissociation of the material as the energy absorbed exceeds the cohesive energy of the lattice [45, 46].

2.2.4 Final state of the ablated material

The final state of the ablated material, i.e. morphology, crystal structure and chemical composition depends on the amount of energy absorbed, material removal mechanism and subsequent cooling rates. Laser beams with near Gaussian spatial profile are usually used for experiments. Hence, the energy deposition is not uniform across sample surface. As a result, density and temperature gradients can be induced and this influences the morphology of the ablated area. By carrying out a postmortem analysis on the irradiated area, characterization of damage threshold fluence dependencies on various features such as: crater profile, crater depth, crater diameter, and local changes in crystallography and chemistry can be related to the

various dynamic mechanisms. For instance, formation of polycrystalline or amorphous regions can be associated with local heating and cooling rates. The generation of crystal defects can be linked to peak pressures developed during ablation. An approximation of the energy deposited can be obtained by analyzing the depth of the ablated crater. Furthermore by analyzing the final state and measuring the fluence of ablated volume the ablation threshold and ablation rates can be estimated.

The postmortem analysis also offers abundance of information pertaining to the practical applications of ultrashort laser pulse in material processing and nanomachining. For example, the interaction of intense femtosecond lasers with material surface results in locally modifying physical state, mechanical, optical, and chemical properties. This confined material changes coupled with the forces that evolve during ablation allows the formation of nanostructure which show potential application in mesoscopic research.

2.3   Multiple Pulse incubation and thermal effects

2.3.1 Incubation effect

For multiple overlapping pulses, increased ablation efficiency can accumulate from pulse to pulse and decrease the damage threshold fluence. The incubation effects only become prominent at repetition rate above 200 kHz.

A study conducted by Rosenfeld *et.al* has shown that the surface damage threshold fluence drops drastically during multiple-laser-shot irradiation, due to material dependent incubation effects (Figure 2–3) [47].
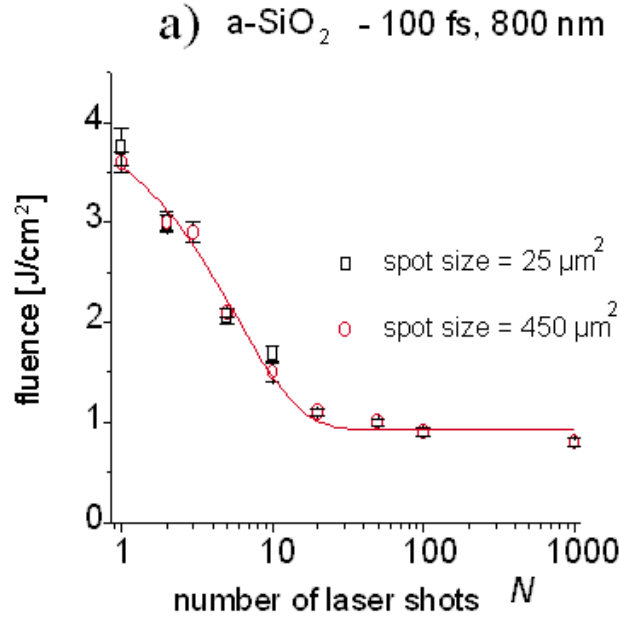
Figure 2–3: Semi-logarithmic plot of the surface threshold vs. shot numbers in fused silica clearly indicating the damage fluence reduction with increased pulse number [47].

The excitation and generation of conduction-band electrons can greatly influence incubation effects in dielectrics leading to an accumulation of defect sites. The multi-photon excitations initially generate the electron-hole pairs on a sub-100 femtosecond time scale. These states last from 150 femtoseconds to several picoseconds [48] before forming self-trapped excitons and Frenkel pairs. A Frenkel pair is a type of point defect in a crystal lattice; a vacancy created when an atom or cation departs from its place in the lattice, resulting in a defect. A small fraction of these Frenkel pairs may not recombine and stabilize to F centers, thereby

introducing additional excitation routes and energy levels for the subsequent laser pulse. With increasing laser pulses striking the surface, the relative change in the laser-induced defect concentration gradually decreases to a point of saturation in dielectrics (Figure 2–3), which corresponds to saturation in threshold fluence.

2.3.2 Thermal Effects

With multiple ultrashot pulses striking the same focal region at high repetition rate (>200 kHz) heat accumulation effects mitigate defect-induced damage and shun collateral damage such as microcracks during laser material processing. Heat accumulation at high repetition rate becomes profound because the time interval between the pulses is less than the time required for the absorbed energy to diffuse out of the focal volume [38, 49, 50]. As the femtosecond laser pulses interact with the substrate, the dielectric material undergoes melting [51] due to heat accumulation. A finite-difference thermal diffusion model developed by Eaton *et.al* predicts that at 1 MHz repetition rate, the temperatures of the focal volume can elevate beyond 3000 ºC due to cumulative heating (Figure 2–4) [52]. This research team employed a laser system that can generate 375 fs at 1 MHz repetition rate with low pulse energy (~5 nJ) to fabricate waveguides in silica and borosilicate glasses.

In general, high laser fluences are required to process transparent dielectrics owing to their wide bandgap (energy difference between the top of the valence band and the bottom of the conduction band). But with MHz repetition rate, processing at lower fluences is possible due heat accumulation with every incoming pulse.
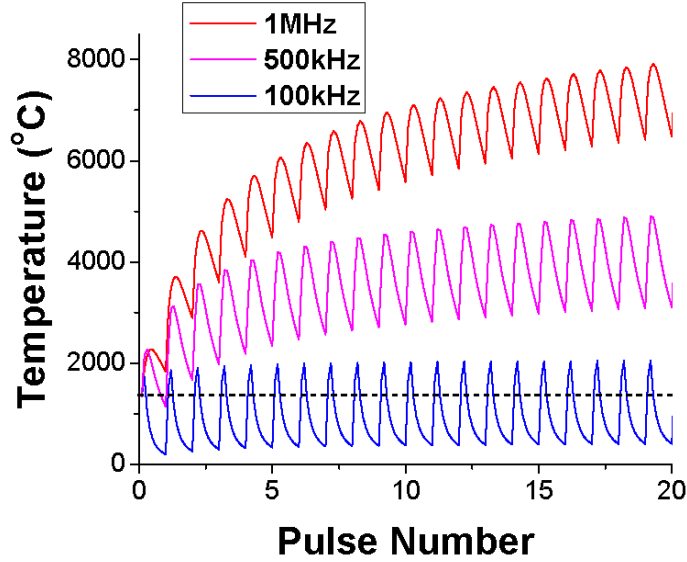
Figure 2–4: A finite-difference model predicting glass temperature for rising pulse number [52].

2.4 Review of glass nanostructures synthesis by femtosecond laser ablation

This section illustrates response of various types of glasses to femtosecond laser irradiation. The current state of research in this field is limited due to lower power levels offered by femtosecond laser systems and low repetition rates (kHz), resulting in the production of only a confined quantity of nanostructures.

2.4.1 Experimental review 1

Ben-Yaker *et.al* investigated the surface morphology by exposing a glass specimen to a single pulse and multiple-pulse femtosecond laser irradiation [53].

The experiment was carried out on a borosilicate glass with composition: 81% SiO_2, 13% B_2O_3, 2% Al_2O_3, 4% Na_2O. Femtosecond laser pulses were obtained from

a regeneratively amplified Ti:sapphire laser. The sample surface was positioned perpendicular to the direction the incident beam.

SEM (Scanning Electron Microscope) image of sample ablated with 100 fs overlapping pulses at an average laser fluence of 0.34 J/mm² and 1 kHz repetition rate is shown in Figure 2–5. The figure clearly demonstrates the formation of thin rims around the crater. A large percentage of deposited energy was being utilized for heating the melting the material. The authors argue that during melt life time, forces acting on the ablated surface shift the molten material from the center to edge of the crater and deposit the melt as thin rim around the ablated area. The flow is caused by hydrodynamic forces due to pressure gradients caused by the plasma that is formed above the molten surface.
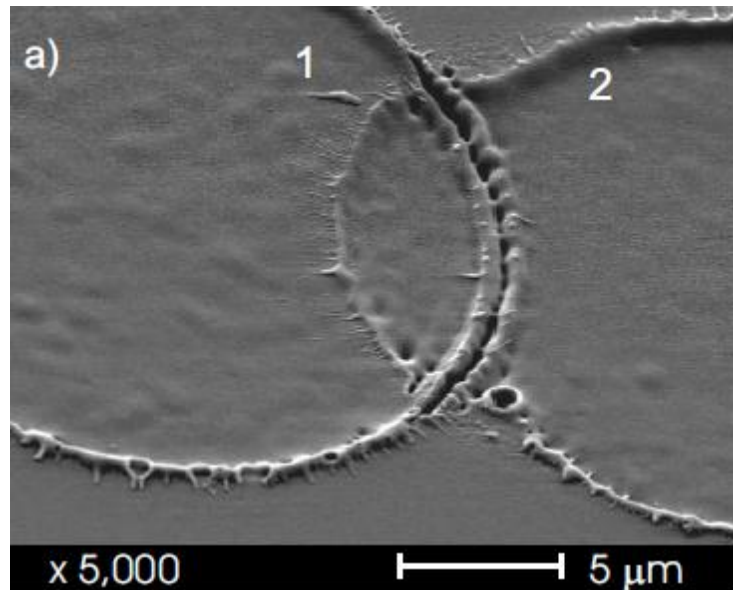
Figure 2–5: Crater rims created by overlapping two laser pulses [53]

2.4.2 Experimental review 2

Juodkazis *et al.* reported the formation of combined nano-fiber-spherical structures by exposing As_2S_3 glass to femtosecond laser pulses at 1 kHz repetition rate in air [54]. The fibers produced were of high aspect ratio and spheres formed were embedded in the fiber with diameters up to several microns.

The femtosecond pulses employed were acquired from Ti:sapphire laser operating at the repetition rate of 1 kHz. The laser beam was focused below the sample surface Figure 2–6. The pulse-duration is 160 fs at fluences larger than 5 J/cm^2.
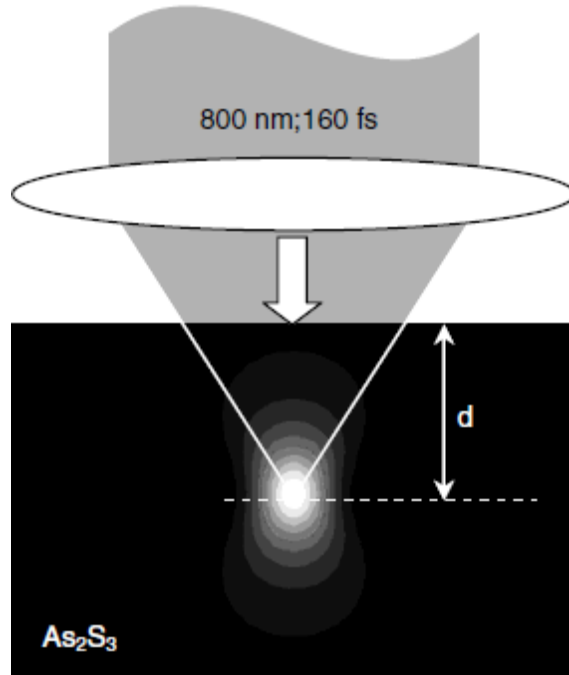
Figure 2–6: The beam was focused at a dept d~6-8 μm from the surface [55].

The morphology of the ablated surface was observed using SEM and is shown in Figure 2–7. The diameters of the obtained fibers ranged from 30 to 300 nm with

lengths up to several millimeters. According to the possible mechanisms proposed by the authors, the formation dynamics is determined by the interacting surface thermo-capillary (Marangoni) forces strongly coupled with thermal processes involved in jet cooling and solidification. The spherical particle formation was associated with liquid jets free energy minimization.
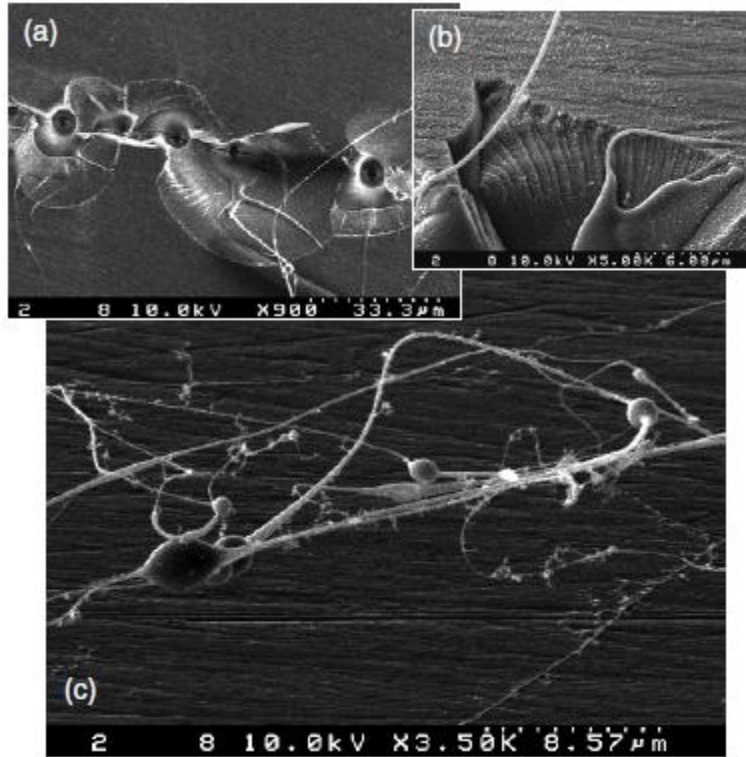
Figure 2–7: SEM image of ablated area with close-up views [55].

2.4.3 Experimental review 3

A Ti:sapphire femtosecond laser with pulse width 183 fs and average power ranging from 1 µJ/pulse to 113 µJ/pulse was employed by Ahsan *et.al* to fabricate micro-holes in fused silica glass [56]. Arrays of micro-holes were drilled with number of pulses at each spot varying from 500 to 3500. Nanostructures like nano-bumps or

nano-pillars along with nano-gratings were observed on the side of the walls and at the bottom of the micro-hole.

Figure 2–8 is the SEM image showing the nano-pillars formation on the side walls and at the bottom of the micro-hole. The dimensions of these pillars were in sub-wavelength range. Nano-gratings were also observed within the micro holes as shown in Figure 2–9. The average period of the nano-grating was determined to be in the range of 175 nm to 200 nm.
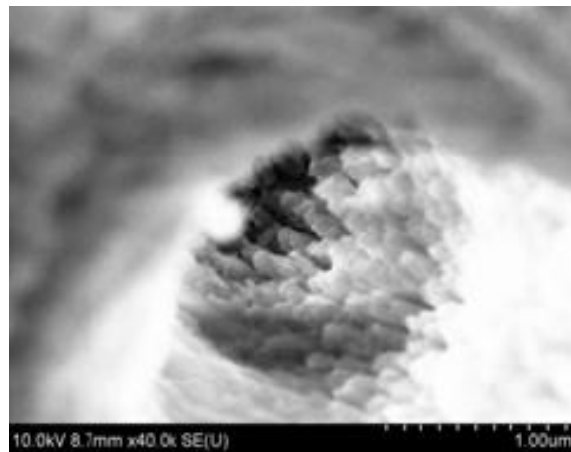
Figure 2–8: Nano-pillars [56]
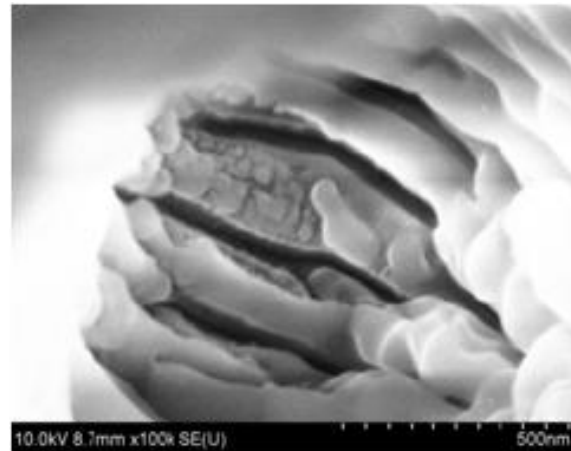
Figure 2–9: Nano-gratings [56]

37

2.5   Summary

A transparent dielectric material when subjected to intense femtosecond laser irradiation, the energy is quickly absorbed via nonlinear mechanisms such as: multiphoton ionization, followed by inverse bremsstrahlung and avalanche ionization, to generate free electron cloud within the conduction band. The electrons upon reaching a critical density undergoes electron-phonon relaxation and the absorbed energy is transferred to the lattice in the order of few picoseconds, which leads to photoinduced damage and decomposition of material into a mixture of microscopic molten droplets and expanding vapor.

The main advantages of using femtosecond lasers for ablation are: (1) The peak intensity of a femtosecond laser can reach to the order of GW/cm^2 or TW/cm^2; (2) heat diffusion into the material is negligible; (3) there is rapid deposition of energy into the material; (4) with multiple pulses the damage threshold fluence is reduced due to heat accumulation and incubation effects. Therefore, femtosecond laser at MHz repetition rate is an ideal tool to process hard to ablate materials (with high bandgap energy) such as transparent glass and generate structures in nanoscale regime.

Chapter 3
Experimental procedures

Experiments were conducted using a direct-diode-pumped Yb-doped fiber oscillator/amplifier femtosecond laser system capable of delivering a maximum output power of 15 W at variable repetition rates ranging from 200 kHz to 25 MHz. The system produces pulses with duration 214 fs with a central wavelength of 1030 nm and circular polarization. A series of UV fused silica plano-convex coated lens with focal lengths 100 mm and 200 mm were used to expand the beam diameter to 8mm. The expanded beam was focused to a spot of diameter 10 μm (on to the target) using a telecentric lens with effective focal length 100 mm. Circular polarization was achieved by aligning a quarter waveplate with the beam. A galvoscanner was used for high speed beam positioning in x-y axis. An optical shutter was used to switch on and off the laser beam. The location of laser focal spot on the target was controlled by using a two-axis precision translation stage with smallest resolution of 1 mm and a range of 15 cm. The pulse repetition rate varies from 2 MHz to 26 MHz internally with computerized selection. EzCAD© software was employed to control the dwell time. Laser powers are measured prior to beam entering the galvoscanner. Figure 3–1 gives the schematic representation of the experimental setup.

The samples used for experiments are a soda-lime glass, (commercially known as Corning® Glass Microscope Slides 0215, the chemical composition is 73%

SiO_2, 14% Na_2O, 7% CaO, 4% MgO, 2% Al_2O_3) and silica glass (96% SiO_2 + trace elements).
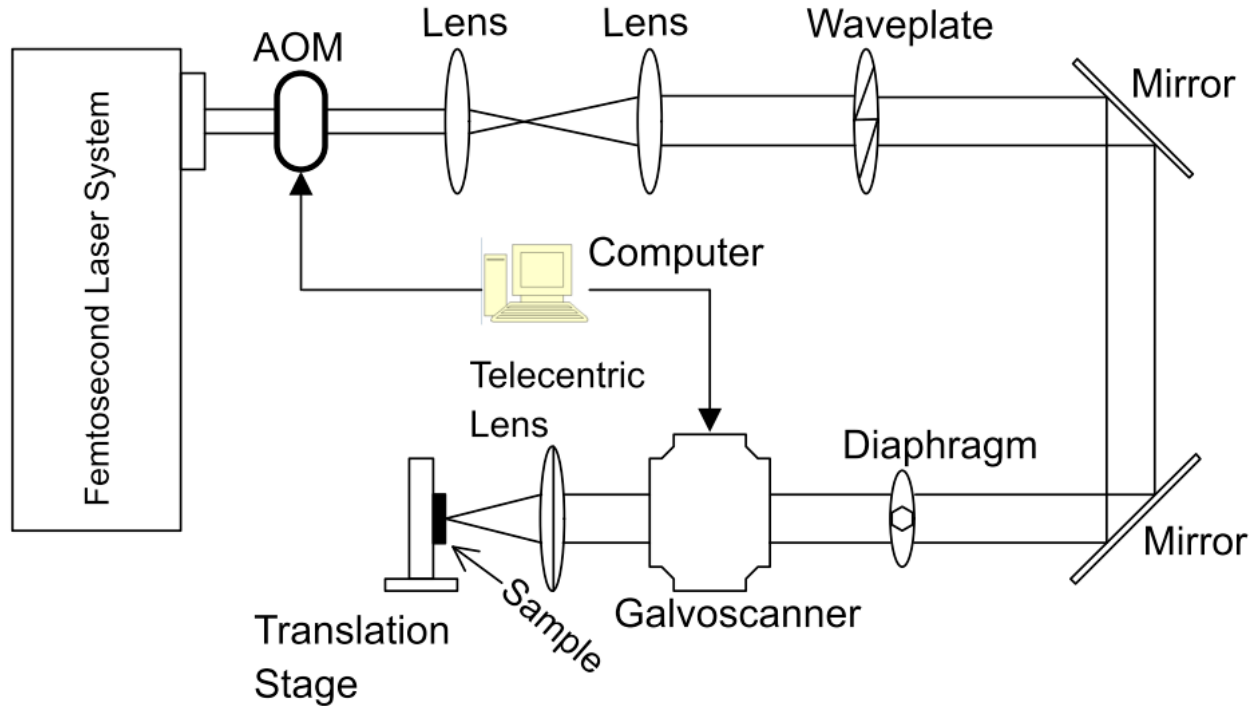
Figure 3–1: Schematic of experimental setup for processing samples with femtosecond laser system. (AOM – Acosto-optic modulator)

An average power delivered to the sample surface is ~11.6 W. Laser beam energy losses were due to reflectively, loss of power in mirrors, and lens absorbing energy along the optical path. Arrays of microvias of 10-30 μm diameter were drilled into the glass sample. Scanning Electron Microscope (SEM) and Transmission Electron Microscopes (TEM) were used to examine and study the laser processed samples.

Chapter 4

Nanofiber Fabrication via Femtosecond Laser Ablation of Silica Glass

4.1   Introduction

This chapter presents the experimental results obtained after ablation of silica glass with femtosecond laser. By irradiating silica glasses surface with a femtosecond laser, densely populated fibers have been obtained with dimension ranging from tens of nanometers to a few hundreds of nanometers for thickness, and up to several millimeters for lengths.

The purpose of this chapter is to put forward a manufacturing technique which can produce nanofibers of varying diameters and lengths on a large scale. Efforts have also been made to shed light on possible mechanisms that promote fiber growth on a silica glass surface when the surface is irradiated with a femtosecond laser.

4.2   Results from femtosecond irradiation of fused silica

4.2.1 Nanostructures

The SEM images shown in Figure 4–1 illustrate the bundled up mass of nanofibers generated on silica glass surface after femtosecond laser ablation. The fibers within the mass are intertwined and randomly oriented over the substrate surface. Several

thousand magnifications (via SEM and TEM) of this mass (Figure 4–2, Figure 4–3) reveals fibers with varying morphologies and diameter distribution. Furthermore, certain fibers attain lengths up to 10 millimeters. The mixture of fibers with different structural characteristics were formed by focusing the laser beam to a spot size of about 10 μm at an average laser fluence of 1.17 J/cm^2 and pulse energy 922.2 nJ. The surface damage threshold fluence of silica was determined experimentally and a fluence value of 0.93 J/cm^2 was obtained. The laser fluence (1.17 J/cm^2) used in our experiments was well over the damage fluence of silica glass. It is believed that there could be more than one mechanism occurring simultaneously or consecutively in the background to produce fibers of different dimensions and morphologies during laser-material interaction. Henceforth, the nanofibers are segregated into different types based on morphology, length and diameter distribution.
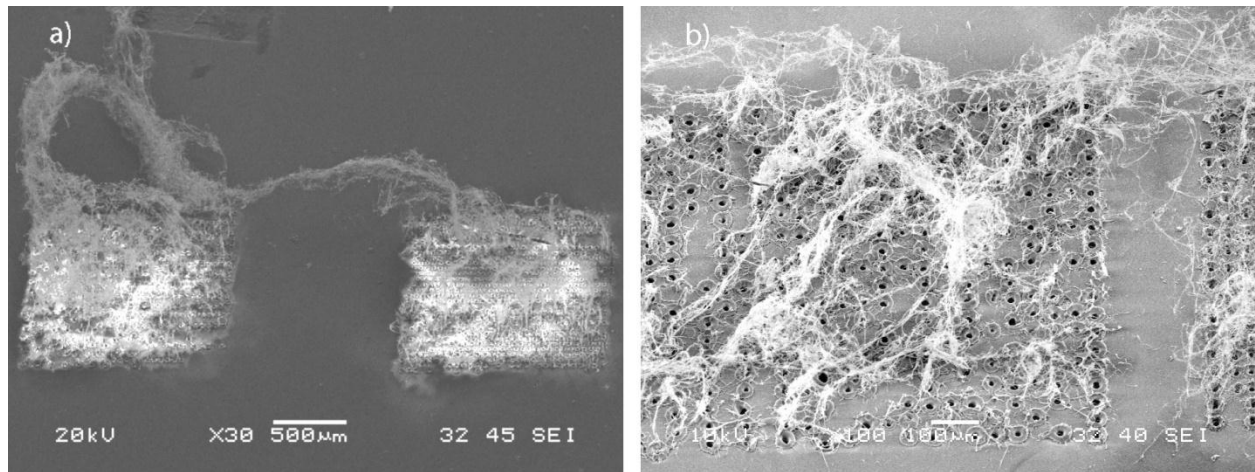
Figure 4–1: a) SEM images of Silica Nanofibers generated at 12.4 MHz and dwell time 5 ms; b) Densely populated nanofibers emerging out around the microholes produced by femtosecond laser.

42

4.2.2 Morphology of Nanofibers

Type 1 fibers (Figure 4–1b) are the longest with lengths from 7 mm and above and with diameter in few hundreds of nanometers. **Type 2** fibers display distinct spherical bead like structures attached along the fiber length (Figure 4–2b). **Type 3** fibers possess dimensions similar to that of Type 1 nanofibers, but have a broadened spherical structure at one end with gradual tapering to the other end (Figure 4–2c). **Type 4** (Figure 4–2d) fibers have their diameters in few tens of nanometers and lengths up to hundreds of microns.
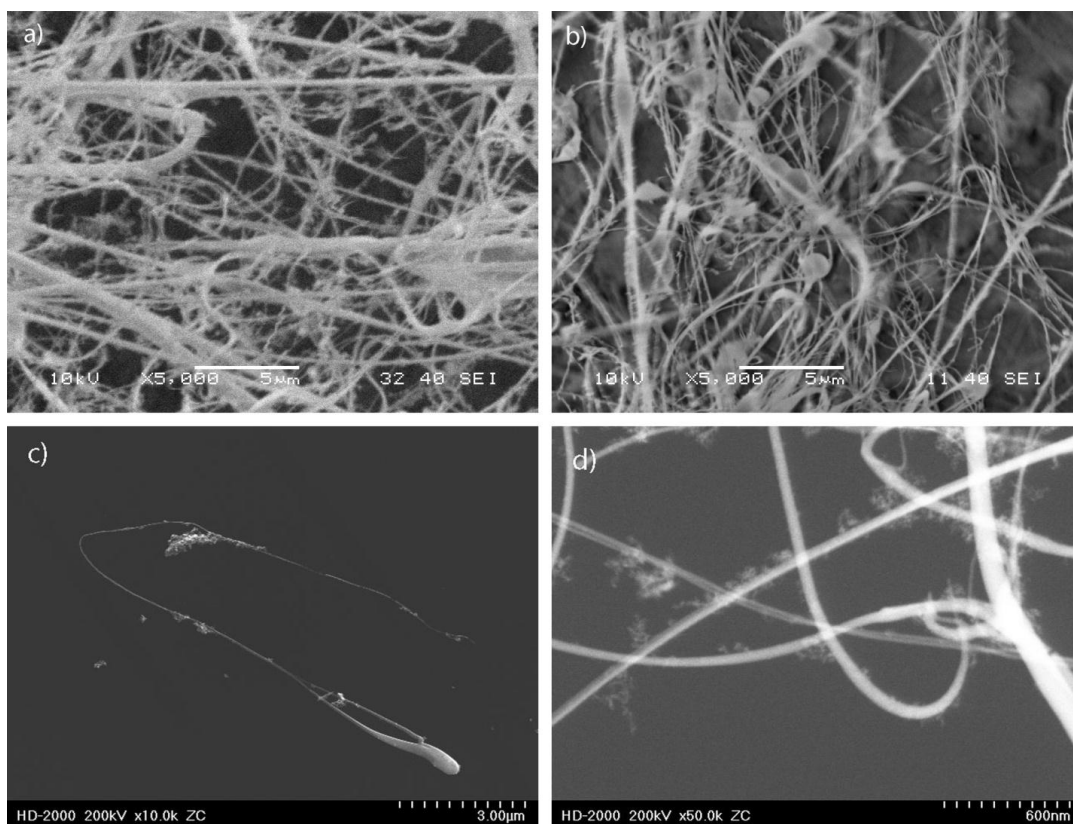
Figure 4–2: Nanofibers of different morphologies a) SEM image of nanofibers with varying diameters and lengths; b) Nanofiber with spherical beads attached; c) TEM image illustrating an expelled droplet transformed into a fiber; d) TEM images silica fibers with nanometer dimensions

Further examination of the TEM micrographs (Figure 4–1) shows the evidence of deposited nanoparticles on the fiber surface. Nanoparticles formation can be explained as the effect of vapor condensation in the rarified plasma. The high temperature of the particles allows the particles to agglomerate (Figure 4–3b) and attach to the fiber surface [57]. A detailed explanation of nanoparticle agglomerate formation is given in Chapter 5 (5.2.2 Nanoparticle production by Laser ablation).
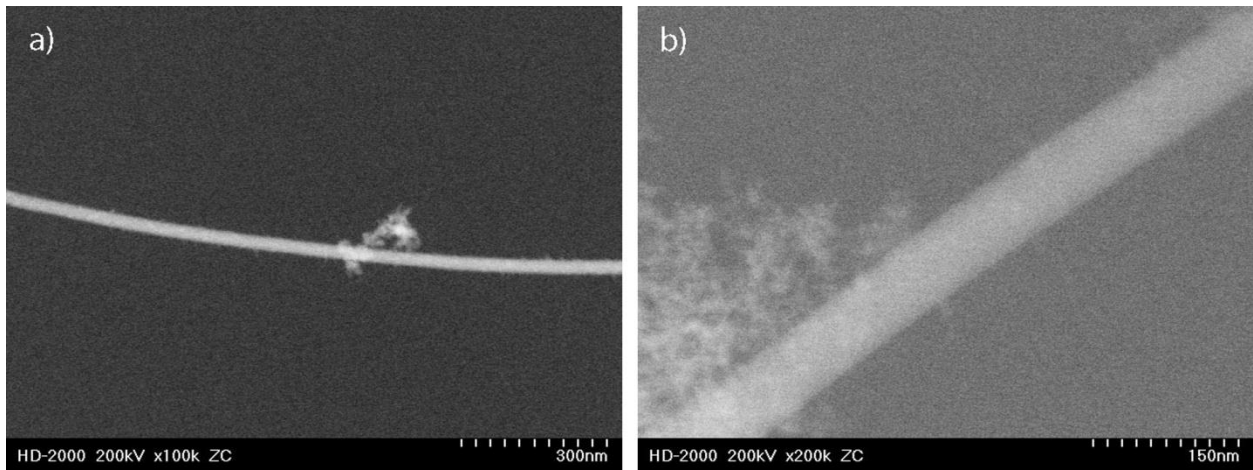
Figure 4–3: TEM image of a nanofiber with diameter less than: a) 50 nm; b) 100 nm

4.3   Discussions

4.3.1 MHz Laser pulses irradiation of dielectric material

The femtosecond laser interaction with transparent dielectric material is a nonlinear absorption process which begins with the formation of free electron cloud in the conduction band within the solid. Ionization process such as: multiphoton ionization, followed by inverse bremsstrahlung and avalanche ionization play a major role in the production of free-electron cloud [33-36]. The free electron density,

upon reaching a critical value triggers the material breakdown process. As the electron subsystem attains thermal equilibrium and undergoes rapid electron-phonon relaxation, energy is transferred into the lattice in the order of few picoseconds [38]. A fraction of this heat energy diffuses into the substrate. But with multiple pulses striking the same focal region at high repetition rate, heat accumulation becomes profound as the time interval between the pulses is less than the time required for the absorbed energy to diffuse out of the focal volume [38, 49, 50]. A finite-difference thermal diffusion model developed by Eaton et al predicts that at MHz repetition rate, the temperatures of the focal volume can elevate beyond 3000 ºC due to cumulative heating [52]. At such high temperatures the viscosity of the molten material is drastically reduced, thereby making it very mobile. Therefore, cumulative heating which leads to a high material temperature plays a vital role during ablation as it (locally) melts the glass surface and enables the ablative forces to restructure the molten material into nanofibers.

4.3.2 Heat conduction at high pulse repetition rate

The use of high repetition (MHz) femtosecond laser pulses causes the surface temperatures to increase beyond melting temperature of the substrate. To validate this claim, a theoretical model was used to estimate the temperature after n pulses.

Assumptions

- No material removal at the end of each pulse

45

- Heating of solid target is in the heat conduction regime, hence losses due to radiation and plume expansion can be neglected

- The laser energy is absorbed in a layer much thinner than the penetration depth of the heat wave. Therefore, the one-dimensional heat diffusion equation can be utilized to model the progression of the heat wave into the target.

$$\frac{\partial T}{\partial t} = a \frac{\partial^2 T}{\partial x^2}$$

Eqn. 4-1

Where:

$$a = k/C_p\rho_0$$

a	Thermal diffusion
k	Heat conduction
C_p	Specific heat
ρ_0	Material density (target)

In order to simplify, the profile of laser pulse is assumed to be in a rectangular shape with step-like rise and fall. By presuming that the energy (heat) flux at the target surface to possess the same temporal form as the absorbed laser flux, the heat conduction Eqn. 4-1 has an exact solution [58, 59]:

$$T(x,t) = k\sqrt{a/\pi} \int_0^{t_p} \frac{I_a(\tau)}{\sqrt{t-\tau}} exp\left\{-\frac{x^2}{2a(t-\tau)}\right\} dt$$

Eqn. 4-2

The average temperature of the heated area of the target from the beginning to the end of the pulse is as follows:

$$T(t) = \frac{1}{\sqrt{at_p}} \int_0^{\infty} T(x, t_p) dx$$

Eqn. 4-3

Where t_p is the laser pulse duration.

For the rectangular shaped pulse the value of the average temperature can be obtained as a function of the laser and target parameters in the explicit form:

$$T(t) = T_m \cdot \sqrt{\left(\frac{t}{t_p}\right)} \qquad \text{Eqn. 4-4}$$

Where T_m is the maximum surface temperature.

It should be noted that the target achieves maximum temperature at the end of the laser pulse, i.e. $T_m = T(0, t_p)$, thus the surface temperature at the center of the spot area during the laser pulse $(t < t_p)$ can be calculated [60, 61]:

$$T(0,t) = T\left(0, t_p\right)\sqrt{\frac{t_p}{t}} = \sqrt{\frac{2}{a}} \frac{I_a(at_p)^{1/2}}{k}\left(\frac{t_p}{t}\right)^{1/2} \qquad \text{Eqn. 4-5}$$

Where I_a is the absorbed laser light intensity which can be estimated from [62].

$$I_a = \frac{4PK(1-R)}{\pi d^2 t_p f} \qquad \text{Eqn. 4-6}$$

Where:

P	Average power
K	Residual energy coefficient
R	Reflection coefficient
d	Spot diameter
f	Frequency

By substituting Eqn. 4-6 in Eqn. 4-5:

$$T_m = T\left(0, t_p\right) = \sqrt{\frac{2a}{\pi^3 t_p}} \frac{4K(1-R)P}{kf d^2} \qquad \text{Eqn. 4-7}$$

The target surface temperature after n laser pulses of pulse duration t_p following with time intervals t_{pp} ($= 1/f$, where f is the pulse repetition rate) can be calculated as follows:

The maximum surface temperature occurs at the end of laser pulse is T_m or $T_{max} = T(0, t_p)$ and T_{min} is the minimum temperature at the beginning of the following laser pulse which is given by $T_{min} = \alpha T_m$. Where α is the constant ratio for the previous maximum and the following minimum temperatures and equal to $\alpha = \sqrt{t_p/t_{pp}}$. From the given relationships, the maximum and minimum temperature of the target surface for n successive pulses can approximated as [58]:

First pulse $\quad (T_{max})_1 = T_m; \qquad\qquad (T_{min})_1 = \alpha T_m$

Second pulse $\quad (T_{max})_2 = (1 + \alpha)T_m; \qquad (T_{min})_2 = \alpha(1 + \alpha)T_m$

nth pulse $\quad (T_{max})_n = (1 + \alpha + \alpha^2 + \alpha^3 + \cdots + \alpha^{n-1})T_m$

$$= [(1 - \alpha^n / 1 - \alpha)]T_m$$

$(T_{min})_n \quad \alpha(T_{max})_n$

The average surface temperature over any ith laser pulse and the time gap between ith and $(i+1)$th can be calculated from

$$\overline{T_n} = \frac{1}{t_p + t_{pp}} \int_0^{t_p + t_{pp}} T_{m,i}(0, t)dt = 2\alpha T_{m,i} \left(\frac{1 - \frac{2}{3}\alpha}{1 + \alpha^2} \right) \qquad \text{Eqn. 4-8}$$

Finally, the average surface temperature after n pulses can be estimated by:

$$\overline{T_n} = \alpha \frac{\left(1 - \frac{2}{3}\alpha\right)}{(1 + \alpha^2)} \frac{T_m}{(1 - \alpha)} \left[1 + \frac{\alpha^n - \alpha}{n(1 - \alpha)}\right] \qquad \text{Eqn. 4-9}$$

In the case $n \gg 1$ and $\alpha \ll 1$

$$\overline{T_n} \cong \alpha T_m = T_m \sqrt{\left(\frac{t_p}{t_{pp}}\right)} \qquad \text{Eqn. 4-10}$$

Hence, the average surface temperature is proportional to the maximum surface temperature T_m obtained at the end of the pulse in a single pulse regime and the square root of the product of the pulse duration t_p and the laser repetition rate [59].

The aforementioned theoretical model was used to calculate the average surface temperature after femtosecond laser irradiation of silica glass with properties given in Table 4-1 and Table 4-2 along with laser parameters given in Table 4-3.

Table 4-1: Thermo physical properties of silica [63]

Thermal conductivity	$k \, (W/m \cdot K)$	2.3
Specific heat	$C_p (J/kg \cdot K)$	740
Density	$\rho_0 (kg/m^3)$	2270

Table 4-2: Silica optical properties [42]

Reflection coefficient	**K**	**0.8**
Residual energy	**R**	**0.7**

Table 4-3: Laser parameters employed

Pulse duration	$t_p(s)$	215×10^{-15}
Frequency	$f(Hz)$	12.4×10^6
Power	$P(W)$	11.6
Spot diameter	$d(m)$	10×10^{-6}
Number of pulses	n	> 30000

By substituting the values (Table 4-1, Table 4-2, and Table 4-3) in Eqn. 4-7 and Eqn. 4-10, a value of **3780** ℃ was computed for the surface temperature.

A finite-difference thermal diffusion model developed by Eaton et al predicts that at MHz repetition rate, the temperatures of the focal volume can elevate beyond 3000°C (Figure 2–5) due to cumulative heating [52]. Therefore the obtained value of 3780 ℃ can be deemed reasonable, but due to the simplifications and assumptions, the calculated average surface temperature is expected to contain a large error. The computed value is not sufficient enough for a quantitative study. The theoretical model employed illustrates that at MHz repetition rate, the surface temperature can reach extremely high temperatures due to multiple-pulse heat incubation.

4.3.3 Mechanisms of nanofiber formation

The process that explains the **Type 1** fiber formation begins with laser pulses striking the surface of substrate (Figure 4–4a) to induce plasma and commence the ablation process that gradually alters the surface morphology. Laser radiation energy is nonlinearly absorbed transferred to the lattice within few picoseconds, after which heat diffusion into material begins [53]. The thermal conductivity of Silica at 1826.85°C is 2.3 W/m-°K [64]. Due to such poor thermal conductivity, significant percentage of laser energy accumulates as heat in the laser irradiated spot with every incoming pulse; consequently, the surface temperature progressively rises in a stepwise fashion [65]. The temperature continues to grow

and begins to melt the material creating a molten pool under the expanding plasma. The molten pool is sustained with the aid of high pulse repetition rate. As the pulse separation time (0.079 µs) is much smaller than melt time of glass (0.4 µs to 0.8 µs) [53]; resolidification of molten material is avoided throughout the irradiation process. The temperature of the molten pool escalates with every inbound pulse; concurrently, the viscosity of the melt reduces progressively making the melt more mobile. Eventually the melt attains viscosity similar to that of a highly mobile liquid at temperatures greater than 3000º C. Under the influence of recoil pressure from the expanding plasma [18, 66] the melt is driven to the edge of the crater where the colder environment surrounding the plasma impedes any further movement of the melt causing it to be deposited as distinct raised rims [67], few micrometers above the surface (Figure 4–4b). The expelled material immediately begins to solidify creating a fine layer of hardened melt which acts as a containing wall (Figure 4–4). The (recently created) molten material continues to be pushed against the containing wall and is ultimately brought under pressure by the ablation forces. The strong temperature gradients induced by the femtosecond laser due to its Gaussian energy distribution, the solidification process of the molten material can be considered non-uniform which leads to the "weak point" areas in the containing wall. The explosive fiber ejection process then can be associated with a breach in the containing wall at the "weak point" [18], causing the hot melt to extrude out as jets. The jet persists as long as melt reservoir is available or the breach seals up. These jets originate at numerous sites over the expelled rims and

as they undergo rapid cooling, alter into densely crowded nanofibers (Figure 4–1b). The above mentioned process could repeat itself multiple times until the expanding crater reaches a final size and the fibers formed prior might get detached and the roots of the fibers melted back into the pool as the melt rim advances.
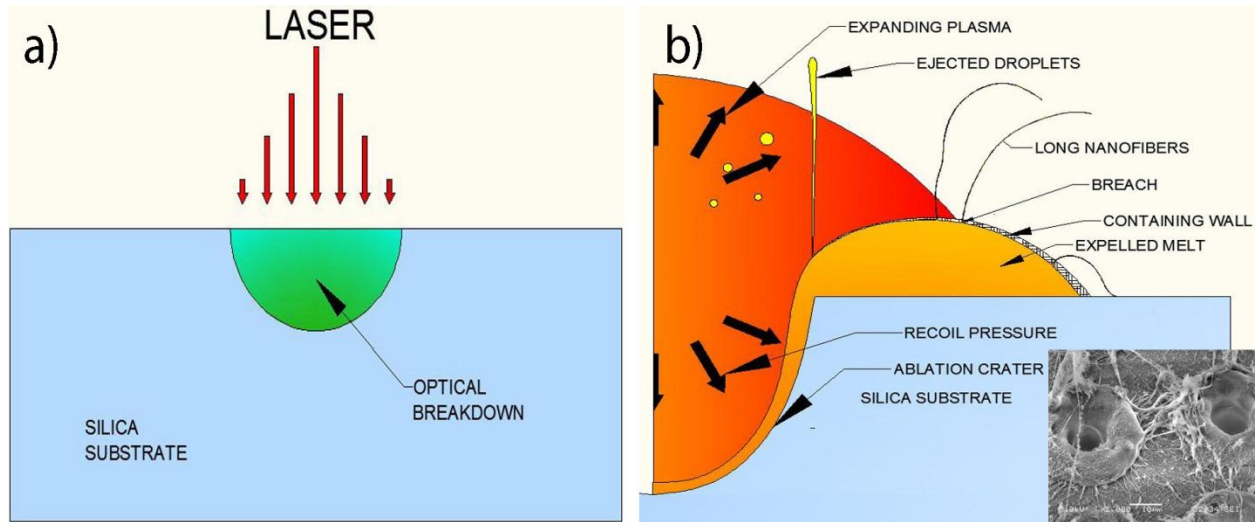
Figure 4–4: a) Optical Breakdown of laser irradiated surface, b) Nanofiber formation process, inset image shows the rim created as result of melt expulsion. Fiber formation during laser ablation is predominantly via melt expulsion followed by generation of molten jets.

A cluster within the produced fibers display distinct spherical bead like structures attached along the length (**Type 2**, Figure 4–5) of the fiber, and can be explained as a consequence of surface destabilization due to laser induced temperature non-uniformity while cooling down and the surface tension minimization of surface area which leads to constricting of jet radius to form beads [55].
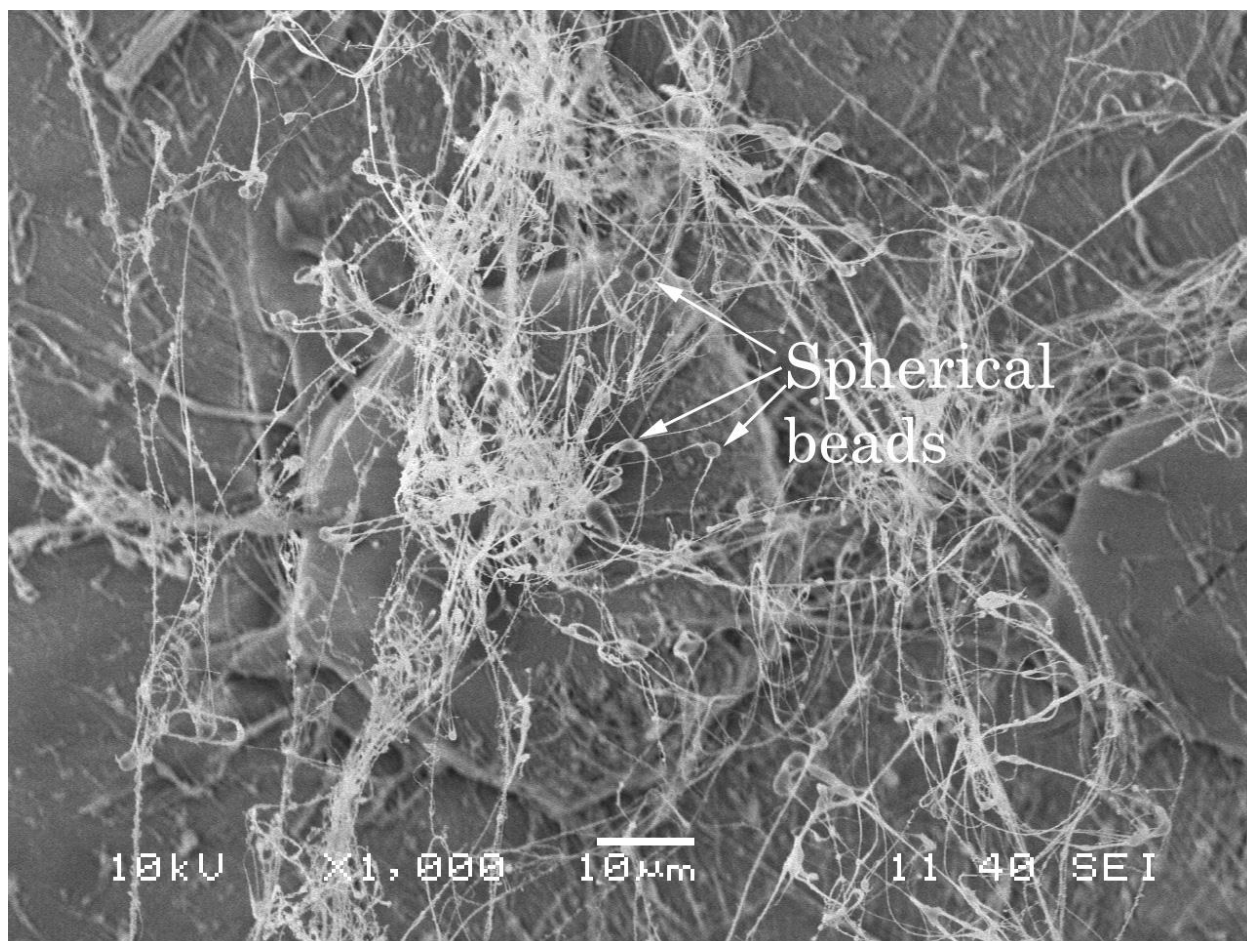
Figure 4–5: Type 2 nanofibers with spherical beads attached to fibers

The silica glass when exposed to femtosecond laser multi-pulse irradiation, rapid heating of specimen occurs causing the glass to melt and the evolving plasma exerts recoil pressure to instigate an expulsion of melt droplets. As the droplets fly out, the volume of the droplet shrinks while leaving a liquid trail behind it. The liquid droplet upon losing momentum cools down and solidifies into a nanofiber (**Type 3,** Figure 4–6).

Figure 4–6: Type 3 nanofibers formed by the expulsion of molten droplet

The growth process for **Type 4** (Figure 4–7) fibers could be similar to the one proposed by Tokarev *et al* [17]. He and his team fabricated nanofibers in PMMA polymer using nanosecond pulsed laser and suggested that the fiber generation is triggered by the formation of energetic droplets within the molten pool created during ablation which then propagate to the periphery of the laser spot due to pressure gradients in the molten liquid and act as heads for the viscous liquid to eject out. The ejected liquid undergoes rapid cooling and is solidified as fibers.

Figure 4–7: Type 4 nanofiber with diameter less than 100 nm

4.4 Summary

A novel method to generate silica nanofibers using femtosecond laser has been presented. This facile, single-step method provides an alternative for the production of nanofiber and sub-micron fibers in large scale with short processing time and the procedure can be carried out in air at ambient conditions. The acquired nanofibers have wide range of diameters. Fibers with thickness below 100 nm were obtained with length reaching up to few hundreds of microns. Based on morphology, fibers were classified into four different types and the associated

possible mechanisms that transpire have been elucidated. The fibers of different types are summarized in Table 4-4. And, the laser parameters utilized are shown in Table 4-5. The predominant process that initiates the fiber growth begins with melting of the substrate, followed by explosive expulsion of the melt by recoil pressure exerted by the expanding plume. The rapid cooling of the expelled material ultimately leads to the formation of nanofibers of extremely high aspect ratio.

Table 4-4: Summary of different types of silica nanofibers

Type of nanofiber	Diameter	Length
Type 1	Few hundreds of nm	> 7 mm
Type 2	50 – 200 nm	Hundreds of microns
Type 3	< 100 nm	Tens of microns
Type 4	< 100 nm	Hundreds of microns

Table 4-5: Laser parameters

Spot diameter	10 μm
Average laser fluence	1.17 J/cm^2
Pulse energy	922.2 nJ
Repetition rate	12.4 MHz
Pulse duration	214 fs
Dwell time	3.0 ms

Chapter 5

Comparison of nanostructures generated on SiO_2 based glass samples after femtosecond laser irradiation

5.1 Introduction

Material response to femtosecond laser differs with types of glass owing to variations in material composition and innate properties. Juodkazis *et al.* reported the formation of combined nano-fiber-spherical structures by exposing As_2S_3 glass to femtosecond laser pulses at 1 kHz repetition rate in air [54]. Ben-Yakar *et al.* irradiated borosilicate glass with femtosecond laser pulses and observed a thin rim of resolidified melt around the crater [53]. During this research work, it was also noticed that with the same regime of laser parameters, various type of glass responded differently. For instance, long continuous nanofibers were obtained from silica glass [68, 69], while interweaved 3D nanopaticle agglomerates were generated from slide glass. Such difference has never been investigated in depth.

This chapter is aimed at studying the distinctive structures of varying morphologies produced on glasses when irradiated under similar experimental laser conditions. Products obtained after the ablation of soda-lime and fused silica were compared. An attempt was made to use difference in bandgap energies to explain the dissimilar responses of glass samples to same laser parameters. The synthesis of nanoparticle agglomerates using femtosecond laser ablation of soda-lime glass at room temperature has also been discussed.

For this study, arrays of microholes were drilled on both glass specimens using laser radiation with a repetition rate of 8.4 MHz, 12.6 MHz, pulse width 214 fs, laser fluence 1.17 J/cm^2, a dwell time 0.5 ms for soda-lime glass and in excess of 3.0 ms for silica glass.

5.2   Results and discussion

5.2.1 Femtosecond laser ablation of soda-lime glass

The SEM image (Figure 5–1) shows the morphology of nanofibrous structure deposited in close vicinity of a microhole created during femtosecond laser ablation at frequencies 8.4 MHz and 12.6 MHz. The structure consists of nanoparticles fused in a web-like pattern. A high magnification image obtained from SEM reveals the size of the particles ranging from 30 nm to 70 nm. The fibrous structure also displays certain degree of porosity. The frequencies and power levels employed for processing the soda-lime glass exceed the threshold for nanoparticle formation. A decrease in particle size was noticed for specimens processed at 12.6 MHz (Figure 5–1b). This is due to the fact that with increased pulse repetition rate, the pulse energy reduces which results in the decrease of nanoparticle sizes. The nanoparticle synthesis via femtosecond laser ablation can be explained by the theory of vapor condensation [70].
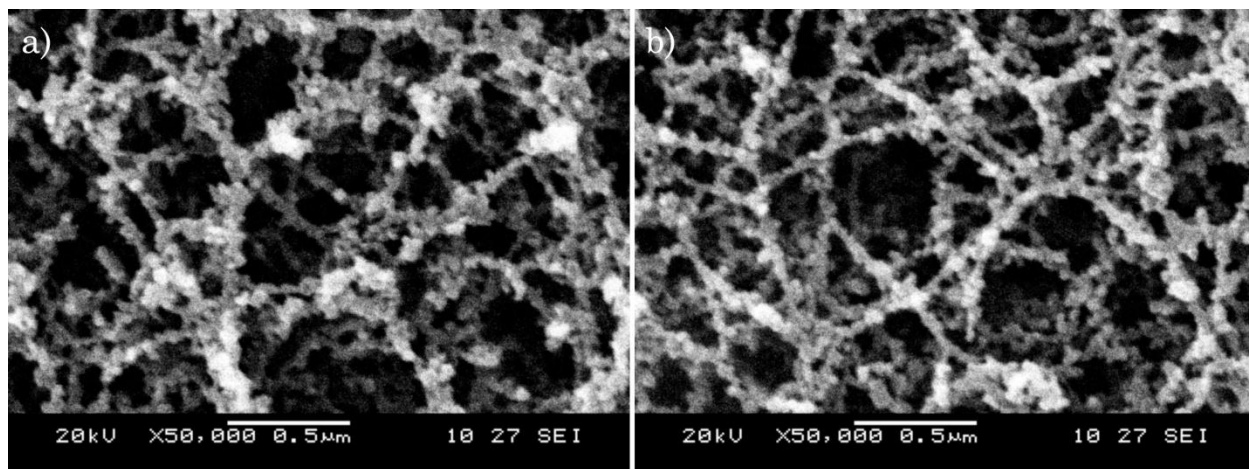
Figure 5–1: Nanoparticle agglomerates on soda-lime glass ablated at (a) 8.4MHz; (b) 12.6 MHz

5.2.2 Nanoparticle production by Laser ablation

Figure 5–2 illustrates the formation process of nanoparticle agglomerates when soda-lime glass is exposed to femtosecond laser irradiation. During the laser ablation the constituents of the expanding laser plume undergo several physical states prior to condensation. In dielectric materials, incident laser energy is absorbed through nonlinear processes (multiphoton and avalanche ionization) by free electrons and the energy is then rapidly transferred to the lattice owing to electron-phonon coupling. Consequently, the lattice attains high temperature leading to a phase transformation (melting of surface, evaporation, and plasma formation). The very high heating rates instigate rapid melting and the transition of melt to an overcritical fluid. An overcritical fluid occurs due to a non-equilibrium state of the material influenced by the effect of high pressure and temperature. Simultaneously, the plume generated above the sample surface expands rapidly into the atmosphere. The plume front at earlier stages is spherical nature but with

59

time the front becomes sharpened and splits into fast and slow moving clouds denoting plume splitting [71-74].

The vaporized target (at high temperature) material within the expanding plume is brought to critical state via a supercooling process (cooling below the freezing point). Supercooling causes the vaporized material inside the plume to form nuclei. The supersaturation of critical vapor within the plume causes the condensation of nuclei and leads to the formation of nanoparticles. The vapor is sustained by the successive laser pulses (at MHz repetition rate) which leads to coalescence of several nuclei and increase the size of the particle. Since the pulse interval is shorter than the cooling time required for complete solidification of nanoparticles, the formed nanoparticles (still in molten sate) agglomerate and fuse into chain-like structures. Finally, the nanoparticles agglomerate in a web-like 3-D pattern as shown in Figure 5–2f. A detailed explanation of the mechanism can be found in references [57, 75].
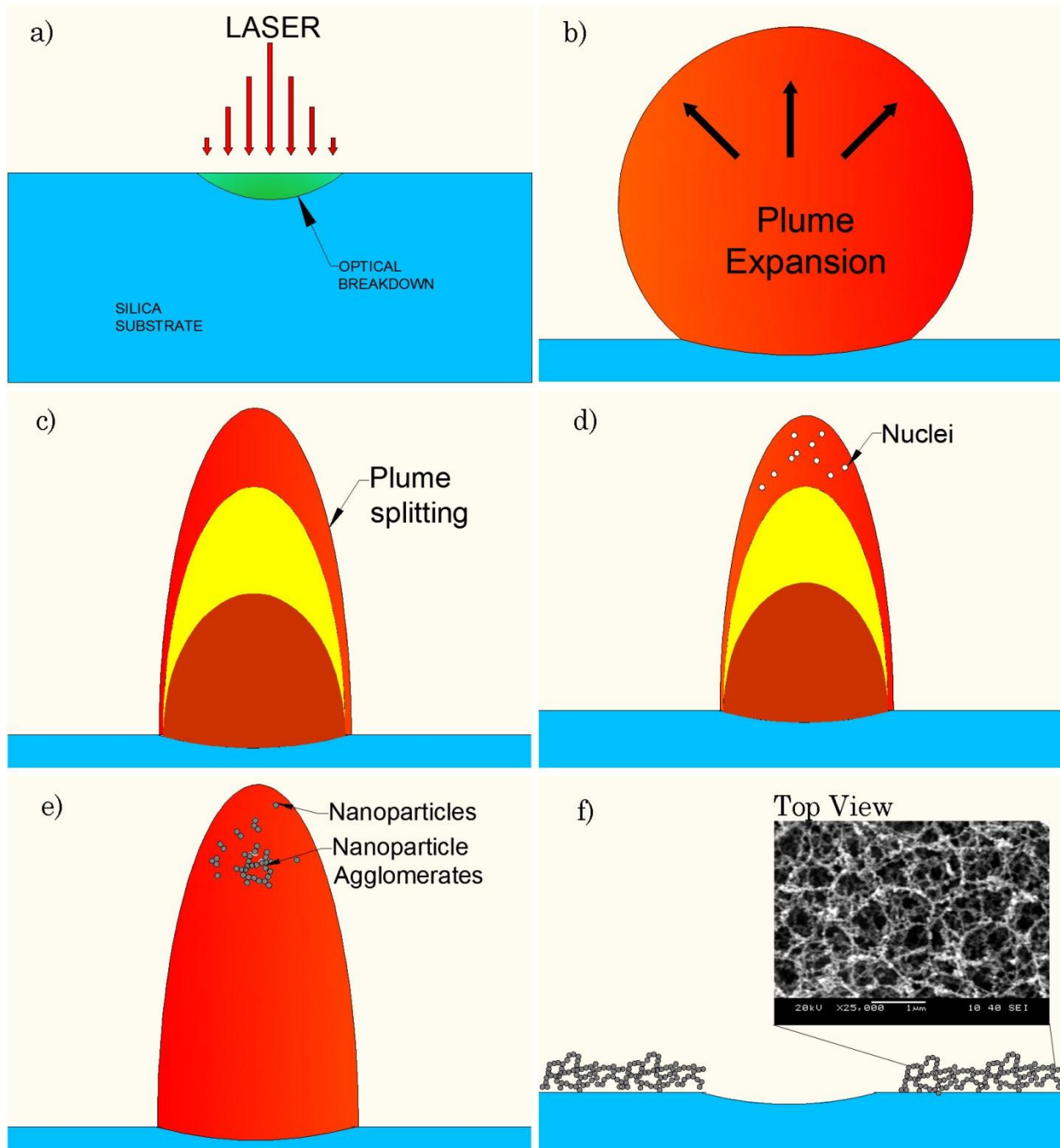
Figure 5–2: Nanoparticle formation process. a) Optical breakdown of laser irradiated surface; b) Plume ignition followed by rapid expansion; c) Plume front sharpening and splitting; d) Nucleation due to supercooling of vapor plume; e) Nanoparticle formation via condensation of nuclei and incomplete coalesce of nanoparticles; f) A 3-D nanoparticle agglomerate deposited on the glass surface.

5.2.3 Femtosecond laser ablation of fused silica glass

The experiment was performed on silica glass with the exact experimental conditions used for soda-lime glass but with dwell time of 5.0 ms. At lower dwell times (0.5-2.0 ms), there was no evidence of nanostructures, but at higher dwell times, formation of nanofibers was observed, implying that silica glass is more difficult to ablate than soda-lime glass. This is due to the fact that silica glass possesses higher bandgap energy than soda-lime glass.

Figure 5–3 shows the produced mixture of fibers with varying structural characteristics. The fibers generated were elongated, continuous and intertwined; the orientation was random over the substrate surface. The fibers had varying morphologies and diameter distribution ranging from few tens of nanometer to hundreds of micrometer. Furthermore, certain fibers attain lengths up to 10 millimeters. Melting of focal volume due to multiple-pulse heat accumulation followed by melt expulsion under the influence of recoil pressure from expanding plasma were determined to be the principal causes for promoting fiber growth on silica glass. The plausible mechanisms that explain the fiber growth has been reported previously [22] and discussed in Chapter 4 (4.3.3 Mechanisms).

Furthermore, a close examination of the fibers with TEM (Transmission Electron Microscope) revealed a nanostructure assembly comprising of agglomerated nanoparticles and nanofibers (Figure 5–3(c)-(d)).
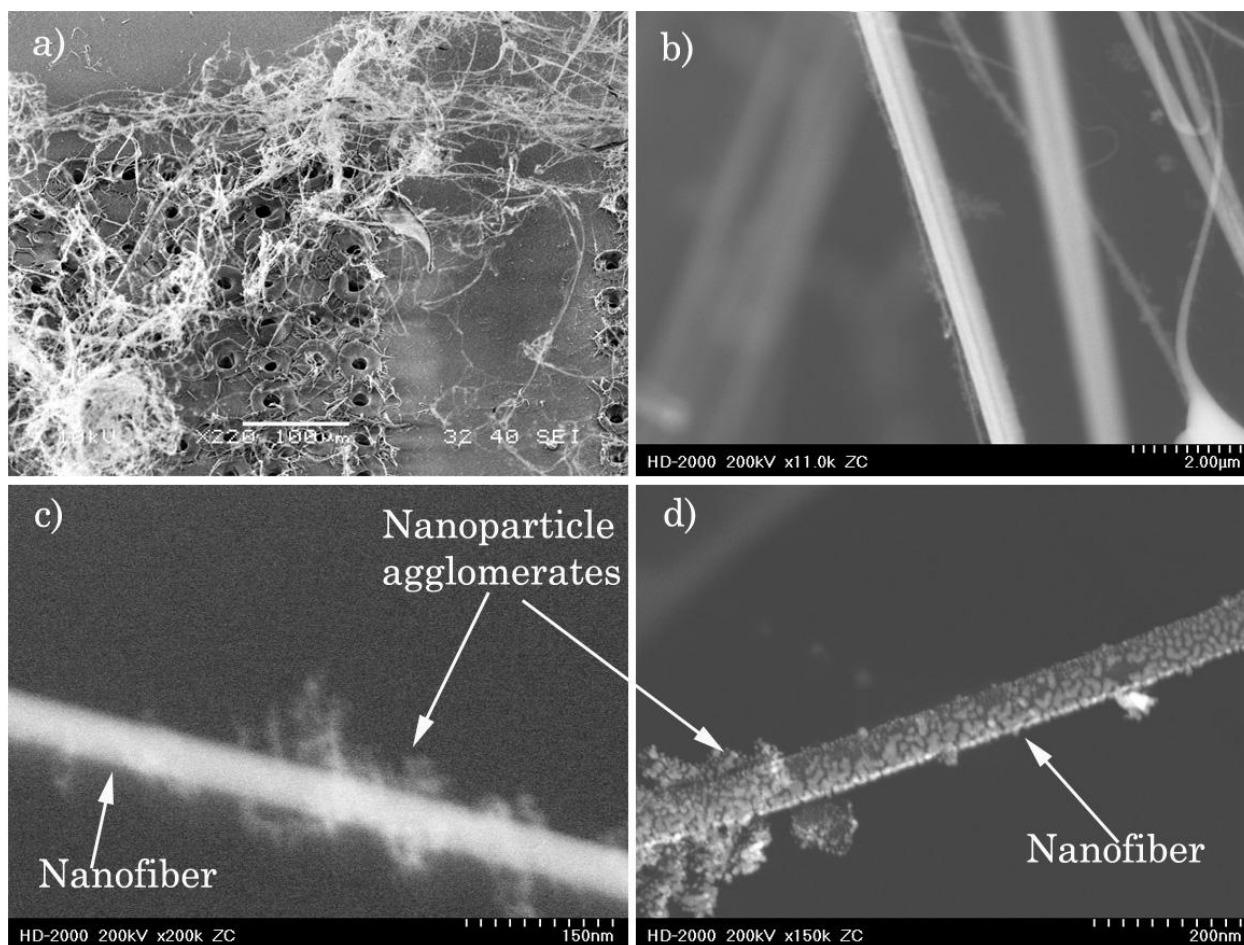
Figure 5–3: a) Densely crowded nanofibers produced around the array of microholes at 12 MHz repetition rate; b) Magnified TEM image of nanofiber; c) TEM image of nanostructure assembly

The combination of vapor condensation and melt expulsion during ablation are the mechanisms responsible for producing such nanostructure assembly on silica glass surface (Figure 5–4).
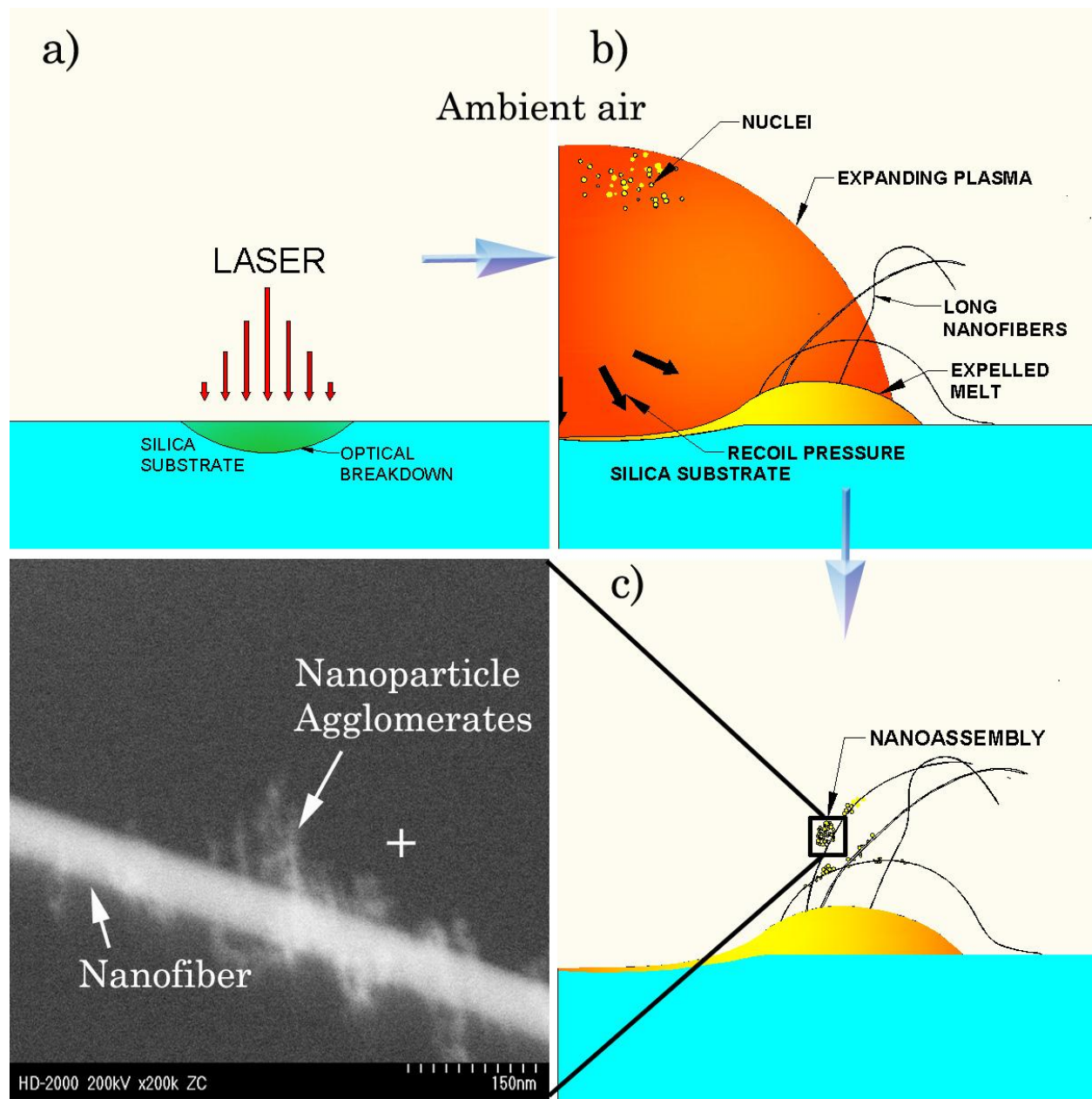
Figure 5–4: Nanoassembly formation process on silica glass; a) Laser optical breakdown; b) As plasma evolves, nucleation and melt expulsion occur; c) Nanostructure assembly on silica glass is the result of a combined effect of: nanofiber formation due to melt expulsion, and nanoparticle agglomeration due to vapor condensation.

The effect of bandgap energy and material composition of different types of glasses in altering the ablation dynamics has been investigated by studying the damage threshold dependence on bandgap and pulse number.

5.2.4 Threshold dependence on bandgap

It is quite evident form literature on femtosecond laser interaction with dielectrics [29, 33, 46, 49, 76]; laser energy absorption process is mainly dependent on the response of electrons to irradiation. Ablation occurs when the free electrons density in the conduction band reaches a critical density. Consequently, to generate the required density of free electrons for breakdown, the valence electrons must overcome band-gap energy to reach the conduction band. Therefore, the band-gap energy has an effect in determining the threshold fluence for ablation. *Mero et al.* have conducted a study to explore the influence of the band gap energy on threshold fluence by exposing five different films (TiO_2, Ta_2O_5, HfO_2, Al_2O_3, and SiO_2) to a femtosecond laser pulse [77]. From the experimental findings, it was shown that the breakdown fluence has approximately linear-dependency on the band gap energy at constant pulse duration. Hence, for a given pulse duration, a material with lower band-gap energy has lower ablation threshold fluence and vice versa.

To verify the dependence of ablation threshold on band-gap an experiment was performed by exposing the soda-lime and silica glass to laser pulses (12 MHz repetition rate) for a dwell time of 0.5 ms at every point in the array. Fluence values of 0.86 J/cm² and 0.93 J/cm² were obtained for soda-lime and silica, respectively.

65

The reduction in fluence value for soda-lime glass can be attributed to its lower band gap (~5 eV [78]) compared to silica glass (~ 9 eV [79]).

5.2.5 Threshold dependence on pulse number

Damage threshold has a strong dependence on the number of pluses interacting with the sample surface. With multiple overlapping pulses, thermal [52] and incubation effects [47] become significant and alter the properties of glass that allows efficient energy coupling by the subsequent pulses. Thus, resulting in lowered ablation threshold and changing the overall ablation dynamics. *Rosenfeld et al.* reported a 70% reduction in surface damage threshold with multiple laser pulses striking the silica surface. The damage threshold decreased from a single-pulse threshold of 3.7 J/cm² to 1.2 J/cm² for 20 laser pulses at 2 Hz repetition rate [47].

To further understand threshold dependence on pulse number. An experiment was carried out on silica and soda-lime glass at 8.4 MHz repetition. For a given pulse number, the laser power was gradually increased until the ablation was attained on glass samples and the corresponding power value were recorded. This process was repeated for various pulse number and the obtained power values were used to calculate the threshold fluence values (Appendix B: MATLAB Code). The plots of acquired results are presented in Figure 5–5. Predictably, the damage threshold fluence values decreased with a rise in pulse number. A reduction of 9.52% was obtained for silica glass with increase in pulse number from 16800 to 42000 and a reduction of 35.15% was identified for soda-lime glass with increase in

pulse number from 840 to 8400. The reduction percentage is significantly higher for soda-lime glass possibly due to higher bandgap of fused silica glass. Furthermore, the presence elements other than Si and O (Figure 5–7(a)) in soda-lime glass allow for improved laser energy absorption compared to silica glass. Thus, fewer pulses are required to ablate soda-lime glass and higher percentage reduction in threshold fluence for successive pulses.
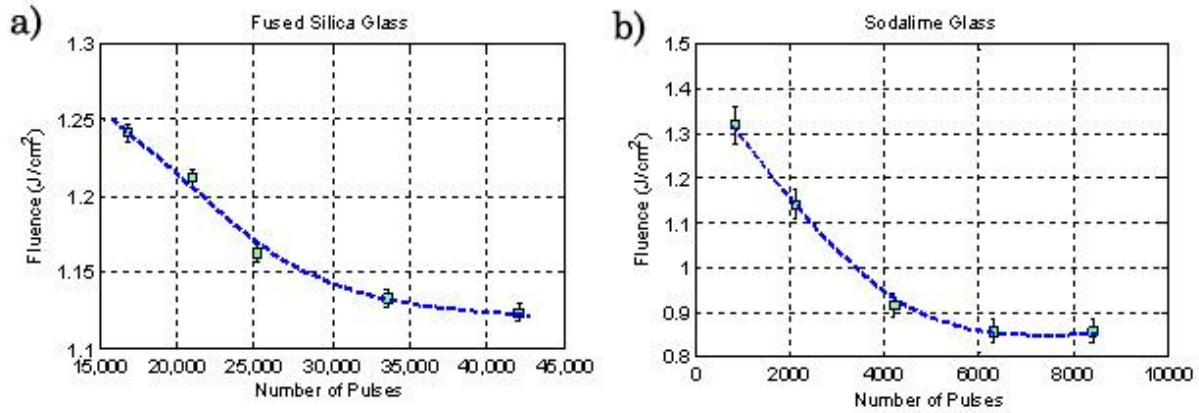
Figure 5–5: Damage threshold fluence dependence on pulse number for silica and soda-lime glass

5.2.6 Comparison of material response to MHz Laser pulses

To understand the material response to femtosecond laser irradiation, series of experiments were conducted. The primary experiment involved ablation of both glasses with laser fluence 1.17 J/cm², dwell time 0.5 ms and at 12.6 MHz repetition rate. The results show the expected nanofibrous structure on soda-lime glass surface (Figure 5–6(a)), but there was no evidence of long nanofiber and particle assembly on silica glass (Figure 5–6(b)). Instead, a rim of expelled melt surrounding

67

the crater was observed. From this experimental result, the following conclusions have been made.

- A dwell time of 0.5 ms is insufficient to produce the nanostructure assembly on silica glass (Figure 5–6b) due to its high bandgap energy (9 eV). Although damage has been induced, the number of pulses striking the glass surface was not sufficient to lower the threshold fluence to the required fluence to create the nanofibers and nano-assembly.

- For silica glass (Figure 5–6b), the material removal is primarily via melt expulsion [53] and only a small percent of material is being removed by vapor-plume expansion. Also, the observed rims around the microhole can explained as the consequence of melt expulsion. Heat accumulation from multiple pulses melts the substrate and the liquefied substrate is expelled out under the influence of recoil pressure from the expanding plasma [18] and deposited as rims few micrometers high above the surface.

- The material removal in soda-lime glass is predominantly via vapor-plume expansion. Soda-lime glass has lower bandgap (5 eV) energy compared to silica glass (9 eV). Therefore fewer pulses are needed to transfer the required amount of free electrons from valance to conduction band to initiate an ablation, thereby, producing a nanoparticle aggregate structure. When multiple pulses strike the surface with high repetition rate constant vapor plume is supplied. With a sustained plume bulk quantities of nuclei are generated within the plume, which

then coalesce and undergo condensation to produce nanoparticles of different sizes [75].
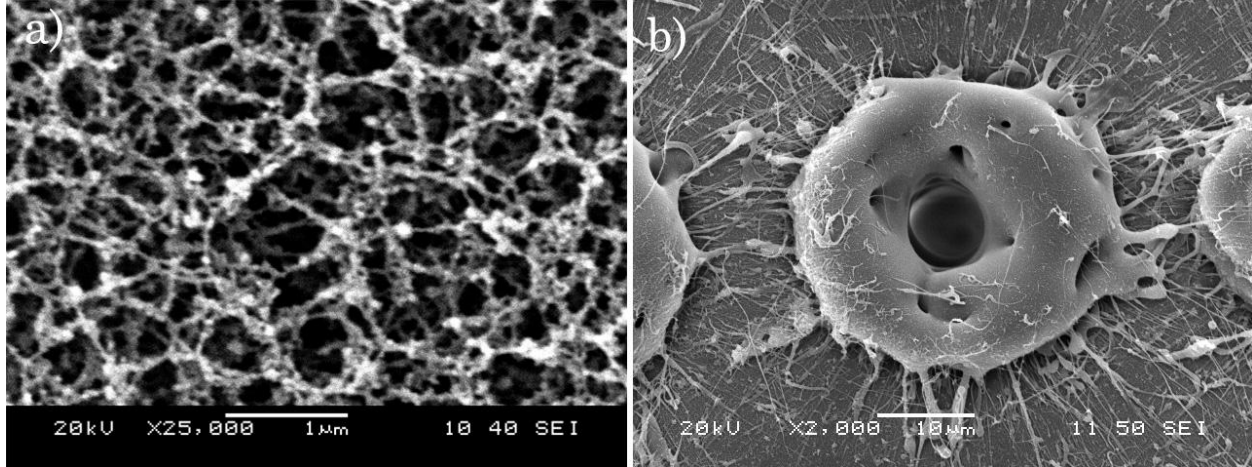
Figure 5–6: (a) soda-lime (b) fused silica ablated with dwell time of 0.5 ms

- The chemical composition of processed and unprocessed soda-lime glass obtained from EDX is shown in Figure 5–7(a)-(b) and it is apparent that the glass specimen is comprised of various elements. Vapor condensation begins with nucleation followed by the growth of supercritical nucleus and finally reaches to a halt due to quenching [70]. As the vapor-plume undergoes condensation during ablation, these elements (e.g. Al, Mg, Ca) may act as catalysts by providing increased nucleation sites within the plume and enhance the nanoparticle production. Al_2O_3 makes only 2% of total composition of unprocessed sample, yet the EDX analysis of nanofiber aggregate (processed sample) shows ~17% (wt%) of Al present in the analyzed area (Figure 5–7(b)). Hence, it can be deduced that Al is the dominant catalytic element that promotes nanoparticle generation.

- The EDX analysis of nanoparticle-and-nanofiber assembly (Figure 5–7(c)) shows just the expected presence of Si and O. Furthermore, the diverse physical and thermal properties cause silica and soda-lime glasses to respond differently to laser irradiation.
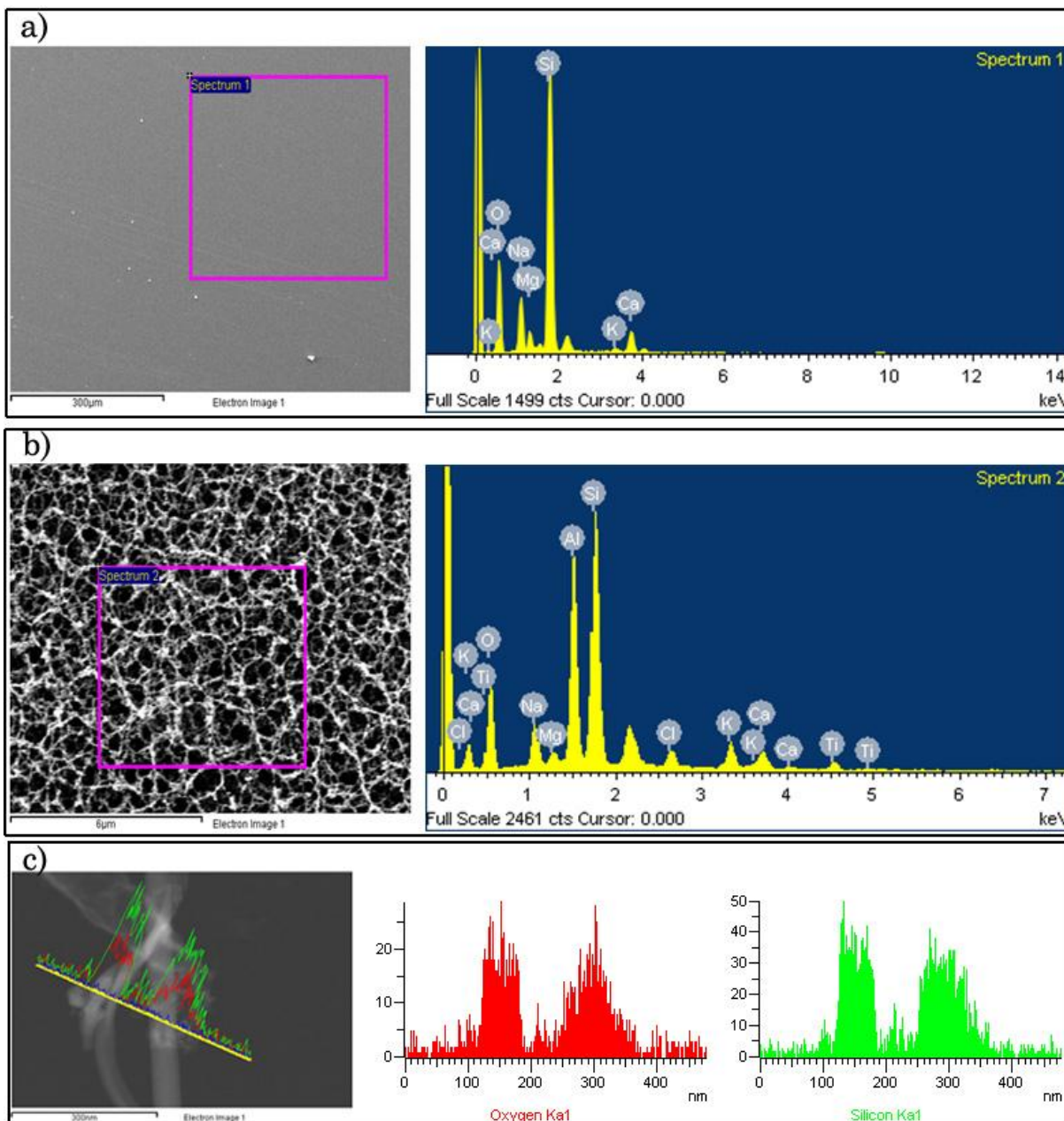
Figure 5–7: EDX of a) unprocessed soda-lime; b) processed soda-lime glass sample; c) EDX of nanofiber-and-nanoparticle assembly (silica)
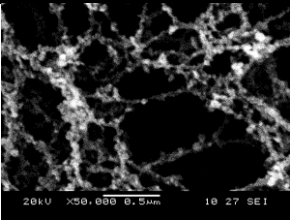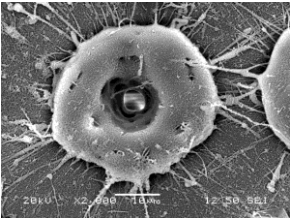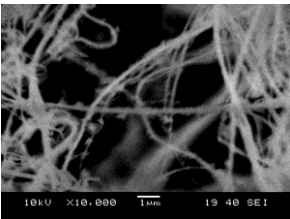
Since there was no evidence of long nanofibers when silica was processed at 0.5ms, another experiment was performed to determine the dwell time required to produce the nanostructure assembly at 12.6 MHz and with fluence 1.17 J/cm^2. A dwell time of 3.0 ms was obtained. For this dwell time, the number of pulses striking the surface is 6 times the number of pulses striking at 0.5 ms. Therefore, the ablation threshold is considerably lowered. Due to poor thermal conductivity of silica, significant percentage of laser energy accumulates as heat in the laser irradiated spot with every incoming pulse; consequently, the surface temperature progressively rises in a stepwise fashion [65]. The temperature continues to grow and begins to melt the material creating a molten pool under the expanding plasma. The melt is restructured into long nanofibers by the ablative forces [22]. Simultaneously, the vapor-plume undergoes nucleation and condensation process leading to the generation of nanoparticles, which are then deposited on previously formed nanofibers creating a nano-assembly (Figure 5–3(c)). When soda-lime glass was ablated under the same laser conditions, severe damage accompanied with cracking on the surface was observed.

5.3   Summary

The response of soda-lime and silica glass to femtosecond laser at MHz repetition rate has been investigated. The nanostructures acquired by ablating both glass types with the same laser parameters possessed distinctly varying morphology. Nanoparticles which fuse to form an interweaving fibrous network structure were

observed on soda-lime glass. An assembly of long continuous fibers and nanoparticle agglomerates was formed on silica glass. A summary of various nanostructures generated is given in Table 5-1. The role of material bandgap that determines the response of glass sample to femtosecond laser irradiation has been studied. Also, the damage threshold fluence dependency on bandgap energy and pulse number was investigated. From the experimental results it was concluded that the material removal in soda-lime glass is dominated by vapor-plume expansion and for silica glass it is dominated by melt expulsion. The different morphology of nanostructures from soda-lime glass and silica glass are caused by the different ablation mechanisms which are in turn influenced by their bandgap energies.

Table 5-1: Summary of nanostructures generated

Nanostructure	Material	Bandgap	Laser parameters		Result
3D-Nanoparticle agglomerates	Soda-lime	~5.0 eV	Frequency	12.6 MHz	
			Power	1.17 J/cm^2	
			Dwell time	0.5 ms	
Expelled rim	Fused silica	~9.0 eV	Frequency	12.6 MHz	
			Power	1.17 J/cm^2	
			Dwell time	0.5 ms	
Long nanofibers	Fused silica	~9.0 eV	Frequency	12.6 MHz	
			Power	1.17 J/cm^2	
			Dwell time	3.0 ms	

Chapter 6

Conclusion and Future work

6.1 Conclusion

Nanostructures have received much attention in the recent years due to their unique properties and potential applications in various areas. The applications of nanostructures spread from nanometric devices in computer chips to the coating of giant industrial components. There are several approaches to generate structures like nanoparticle and nanofibers. This dissertation puts forth a novel fabrication method that generates nanostructures on SiO_2 based glass with configurations such as: a) Long continuous nanofibers of extremely high aspect ratio (certain fibers up to 100000:1) on silica (96% SiO_2 + trace elements) glass surface; b) Nanofiber-and-nanoparticle assembly on silica glass; c) 3-Dimensional nanoparticle agglomerates on soda-lime (73% SiO_2 + other compounds) glass; by ablating glass samples with femtosecond laser at MHz pulse repetition rate under ambient conditions. To the knowledge of the author, using a femtosecond pulsed laser at MHz repetition to generate such unique nanostructures on glass samples has never been reported.

Since the obtained silica nanofibers have extremely high aspect ratios, these fibers can be employed in the production of nano-sensors which may offer advantages of high sensitivity, fast response, small footprints, high spatial resolution, and low detection limits [80]. Henceforth, these nano-sensors can be installed on vehicles for space exploration and satellites, as they require precise

73

measurements of velocity, acceleration, position, and temperature. The three-dimensional nanoparticle aggregate from soda-line glass can be employed in the production nanocomposites with special physical and mechanical properties. These structures also can serve as mechanical supports and tissue scaffolds for cell proliferation.

This research work also investigates the mechanisms that promote nanofibers and nanoparticle agglomerates. The predominant process that initiates the fiber growth on silica glass begins with melting of the substrate, followed by explosive expulsion of the melt by recoil pressure exerted by the expanding plume. The rapid cooling of the expelled material ultimately leads to the formation of nanofibers of extremely high aspect ratio. Vapor condensation during ablation was determined to be the primary cause for particle agglomeration of soda-lime glass.

The dissimilarities in morphology of nanostructure produced on silica and soda-lime glasses have been explained by taking into account the differences in bandgap energies and its role in ablation dynamics. The effect of bandgap and pulse number on threshold fluence was studied.

The results presented in this thesis have not been reported previously and the author believes the research findings will make significant contributions to the better understanding of femtosecond laser ablation of glass materials. The main contributions of this research work are summarized below.

- Reported the synthesis of nanofibers in large quantity via femtosecond laser ablation; and mechanisms that produce such structures using existing models

- Reported the distinctly different responses and products of pure silica (pure SiO_2) and soda-lime (73% SiO_2 + other compounds) glass when irradiated with laser pulses of the same parameters (frequency, fluence, pulse duration, dwell time)

- The difference in bandgap energies of fused silica and soda-lime glass was used to explain the dissimilar responses to laser pulse irradiation. And the supporting experimental evidences was provided

6.2   Future work

The nanofibers obtained on silica glass via femtosecond laser ablation are densely populated, randomly oriented and intertwined, which renders the study of individual fiber quite challenging. In this regard, ways to align the fiber array and to isolate an individual fiber must be extensively explored to carry out a characterization study and to evaluate mechanical properties using analyzing tools such as Atomic Force Microscopy.

Furthermore, the influence of varying laser parameters (repetition rate, pulse duration, dwell time, and laser power) on nanoparticle diameter distribution and porosity of nanoparticle agglomerates on soda-lime glass should be investigated. Image analysis also can be employed to precisely extract information pertaining to particle size from SEM and TEM images.

The difference in morphology of nanostructures obtained on silica and soda-lime were only explained by taking into consideration the variations in bandgap

energies. Therefore, to obtain a thorough understanding about variations in nanostructures of silica and soda-lime glass; a detailed study on the influence of physical and chemical property variation on ablation dynamics during femtosecond laser interaction is suggested.

Appendix A: List of publications

1. Krishnan Venkatakrishnan, **Dheeraj Vipparty**, and Bo Tan, "Nanofibre fabrication by femtosecond laser ablation of silica glass," Opt. Express **19**, 15770-15776 (2011)

2. **Dheeraj Vipparty**, Bo Tan, and Krishnan Venkatakrishnan, "Single-step synthesis of nanostructures on transparent dielectric glasses using a femtosecond laser", Nano Research (Under review)

Appendix B: MATLAB Code

Damage threshold fluence calculations

```
clear all

% Loading data for best fit lines
load Ana1
load Ana2

Data_FS=[12.6 12.3 11.8  11.5  11.4;2 2.5 3 4 5];
Data_SL=[13.4 11.6 9.3 8.7 8.69; 0.1 0.25 0.5 0.75 1.0];

Fl_FS=(4/(8.4e6*pi*(10e-4)^2)).*(Data_FS(1,:).*0.65);
Fl_SL=(4/(8.4e6*pi*(10e-4)^2)).*(Data_SL(1,:).*0.65);

Np_FS=(8.4e6*1e-3).*Data_FS(2,:);
Np_SL=(8.4e6*1e-3).*Data_SL(2,:);

Er_FS=0.005*Fl_FS;
Er_SL=0.03*Fl_SL;
% figure;
% Silica Glass
% subplot(1,2,1)
figure;
h=errorbar(Np_FS,Fl_FS,Er_FS,'ks','MarkerFaceColor',[.49 1
.63],'MarkerSize',5);
hold on
plot(Ana1.xi,Ana1.yfit,'--b','LineWidth',1.5);
title('Fused Silica Glass');
xlabel('Number of Pulses');
ylabel('Fluence (J/cm^2)');
grid on
errorbar_tick(h);

% Sodalime
% subplot(1,2,2)
figure;
h=errorbar(Np_SL,Fl_SL,Er_SL,'ks','MarkerFaceColor',[.49 1
.63],'MarkerSize',5);
hold on
plot(Ana2.xi,Ana2.yfit,'--b','LineWidth',1.5);
title('Sodalime Glass');
xlabel('Number of Pulses');
ylabel('Fluence (J/cm^2)');
grid on
errorbar_tick(h);
hold off
% percentage change
P_FS=((Fl_FS(1)-Fl_FS(end))/Fl_FS(1))*100;
P_SL=((Fl_SL(1)-Fl_SL(end))/Fl_SL(1))*100;
```

References

[1] M. Ineke and T. Malsch, Eds., *Nanoforum - Publications - Nanotechnology in Aerospace -* (http://www.nanoforum.org/nf06~modul~showmore~folder~99999~scid~451~.html?action=longview_publication& ed.) *2011(7/20/2011).*

[2] Y. Xia, P. Yang, Y. Sun, Y. Wu, B. Mayers, B. Gates, Y. Yin, F. Kim and H. Yan, "One-dimensional nanostructures: synthesis, characterization, and applications," *Adv. Mater.,* vol. 15, pp. 353-389, 2003.

[3] G. Cao, *Nanostructures & Nanomaterials: Synthesis, Properties & Applications.* Imperial College Pr, 2004.

[4] G. Brambilla, "Optical fibre nanowires and microwires: a review," *Journal of Optics,* vol. 12, pp. 043001, 2010.

[5] Z. M. Huang, Y. Z. Zhang, M. Kotaki and S. Ramakrishna, "A review on polymer nanofibers by electrospinning and their applications in nanocomposites," *Composites Sci. Technol.,* vol. 63, pp. 2223-2253, 2003.

[6] L. Tong and E. Mazur, "Glass nanofibers for micro- and nano-scale photonic devices," *J. Non Cryst. Solids,* vol. 354, pp. 1240-1244, 2/15, 2008.

[7] R. Vasita and D. S. Katti, "Nanofibers and their applications in tissue engineering," *International Journal of Nanomedicine,* vol. 1, pp. 15, 2006.

[8] S. Sundararajan, B. Bhushan, T. Namazu and Y. Isono, "Mechanical property measurements of nanoscale structures using an atomic force microscope," *Ultramicroscopy,* vol. 91, pp. 111-118, 2002.

[9] L. Tong, R. R. Gattass, J. B. Ashcom, S. He, J. Lou, M. Shen, I. Maxwell and E. Mazur, "Subwavelength-diameter silica wires for low-loss optical wave guiding," *Nature,* vol. 426, pp. 816-819, 2003.

[10] G. Brambilla, F. Xu, P. Horak, Y. Jung, F. Koizumi, N. P. Sessions, E. Koukharenko, X. Feng, G. S. Murugan and J. S. Wilkinson, "Optical fiber nanowires and microwires: fabrication and applications," *Advances in Optics and Photonics,* vol. 1, pp. 107-161, 2009.

[11] L. TONG and E. MAZUR, "TAPER-DRAWING FABRICATION OF GLASS NANOWIRES," in ***Nanofabrication: Fundamentals and Applications***, A. TSENG, Ed. World Scientific Pub Co Inc, 2008, pp. 213.

[12] T. Subbiah, G. Bhat, R. Tock, S. Parameswaran and S. Ramkumar, "Electrospinning of nanofibers," *J Appl Polym Sci,* vol. 96, pp. 557-569, 2005.

[13] S. Ramakrishna, *An Introduction to Electrospinning and Nanofibers.* World Scientific Pub Co Inc, 2005.

[14] D. Li and Y. Xia, "Electrospinning of nanofibers: Reinventing the wheel?" *Adv. Mater.,* vol. 16, pp. 1151-1170, 2004.

[15] S. S. Choi, S. G. Lee, S. S. Im, S. H. Kim and Y. L. Joo, "Silica nanofibers from electrospinning/sol-gel process," *J. Mater. Sci. Lett.,* vol. 22, pp. 891-893, 2003.

[16] X. Wu, W. Song, K. Wang, T. Hu, B. Zhao, Y. Sun and J. Du, "Preparation and photoluminescence properties of amorphous silica nanowires," *Chem. Phys. Lett.,* vol. 336, pp. 53-56, 2001.

[17] V. N. Tokarev, S. Lazare, C. Belin and D. Debarre, "Viscous flow and ablation pressure phenomena in nanosecond UV laser irradiation of polymers," *Appl. Phys. A:Mater. Sci. Process.,* vol. 79, pp. 717-720, 2004.

[18] G. A. J. Markillie, H. J. Baker, F. J. Villarreal and D. R. Hall, "Effect of vaporization and melt ejection on laser machining of silica glass micro-optical components," *Appl. Opt.,* vol. 41, pp. 5660-5667, 2002.

[19] M. T. Swihart, "Vapor-phase synthesis of nanoparticles," *Curr. Opin. Colloid Interface Sci.,* vol. 8, pp. 127-133, 3, 2003.

[20] J. -. Yu, C. -. Lee, S. -. Im and J. -. Lee, "Structure and magnetic properties of SiO2 coated Fe 2O3 nanoparticles synthesized by chemical vapor condensation process," *Rev. Adv. Mater. Sci.,* vol. 4, pp. 55-59, 2003.

[21] H. H. Kung and E. I. Ko, "Preparation of oxide catalysts and catalyst supports — a review of recent advances," *Chem. Eng. J Bioch. Eng.,* vol. 64, pp. 203-214, 11, 1996.

[22] M. Zawrah, A. El-Kheshen and H. M. Abd-Elaal, "Facile and economic synthesis of silica nanoparticles," *Journal of Ovonic Research Vol,* vol. 5, pp. 129-133, 2009.

[23] R. Mueller, L. Mädler and S. E. Pratsinis, "Nanoparticle synthesis at high production rates by flame spray pyrolysis," *Chem. Eng. Sci.,* vol. 58, pp. 1969-1976, 5, 2003.

[24] J. J. Gonzalez, C. Liu, S. -. Wen, X. Mao and R. E. Russo, "Glass particles produced by laser ablation for ICP-MS measurements," *Talanta,* vol. 73, pp. 577-582, 2007.

[25] K. Saulig-Wenger, D. Cornu, F. Chassagneux, T. Epicier and P. Miele, "Direct synthesis of amorphous silicon dioxide nanowires and helical self-assembled nanostructures derived therefrom," *J.Mater.Chem.,* vol. 13, pp. 3058-3061, 2003.

[26] Y. Q. Zhu, N. Grobert, H. Terrones, J. P. Hare, H. W. Kroto, W. K. Hsu, M. Terrones and D. R. M. Walton, "3D Silicon oxide nanostructures: from nanoflowers to radiolaria," *J. Mater. Chem.,* vol. 8, pp. 1859-1864, 1998.

[27] J. L. Gole, J. Stout, W. L. Rauch and Z. Wang, "Direct synthesis of silicon nanowires, silica nanospheres, and wire-like nanosphere agglomerates," *Appl. Phys. Lett.,* vol. 76, pp. 2346, 2000.

[28] Z. Wang, R. Gao, J. Gole and J. Stout, "Silica nanotubes and nanofiber arrays," *Adv. Mater,* vol. 12, pp. 1938-1940, 2000.

[29] E. Gamaly, A. Rode, B. Luther-Davies and V. Tikhonchuk, "Ablation of solids by femtosecond lasers: Ablation mechanism and ablation thresholds for metals and dielectrics," *Phys. Plasmas,* vol. 9, pp. 949, 2002.

[30] X. Liu, D. Du and G. Mourou, "Laser ablation and micromachining with ultrashort laser pulses," *IEEE J. Quantum Electron.,* vol. 33, pp. 1706-1716, 1997.

[31] A. Zoubir, L. Shah, K. Richardson and M. Richardson, "Practical uses of femtosecond laser micro-materials processing," *Appl. Phys. A,* vol. 77, pp. 311-315, 2003.

[32] A. Kaiser, B. Rethfeld, M. Vicanek and G. Simon, "Microscopic processes in dielectrics under irradiation by subpicosecond laser pulses," *Phys. Rev. B,* vol. 61, pp. 11437, 2000.

[33] M. Feit, A. Komashko and A. Rubenchik, "Ultra-short pulse laser interaction with transparent dielectrics," *Appl. Phys. A:Mater. Sci. Process.,* vol. 79, pp. 1657-1661, 2004.

[34] S. Chin, "From multiphoton to tunnel ionization," *Advances in Multi-Photon Processes and Spectroscopy,* vol. 16, pp. 249, 2004.

[35] A. Kaiser, B. Rethfeld, M. Vicanek and G. Simon, "Microscopic processes in dielectrics under irradiation by subpicosecond laser pulses," *Physical Review B,* vol. 61, pp. 11437, 2000.

[36] A. Brodeur and S. Chin, "Band-gap dependence of the ultrafast white-light continuum," *Phys. Rev. Lett.,* vol. 80, pp. 4406-4409, 1998.

[37] M. Lenzner, "Femtosecond laser-induced damage of dielectrics," *Internat. J. Modern Phys. B,* vol. 13, pp. 1559-1578, 1999.

[38] F. Korte, J. Koch and B. Chichkov, "Formation of microbumps and nanojets on gold targets by femtosecond laser pulses," *Appl. Phys. A:Mater. Sci. Process.,* vol. 79, pp. 879-881, 2004.

[39] Y. Yamashita, T. Yokomine, S. Ebara and A. Shimizu, "Heat transport analysis for femtosecond laser ablation with molecular dynamics-two temperature model method," *Fusion Eng. Des.,* vol. 81, pp. 1695-1700, 2006.

[40] R. Stoian, M. Boyle, A. Thoss, A. Rosenfeld, G. Korn, I. Hertel and E. Campbell, "Laser ablation of dielectrics with temporally shaped femtosecond pulses," *Appl. Phys. Lett.,* vol. 80, pp. 353, 2002.

[41] F. Ladieu, P. Martin and S. Guizard, "Measuring thermal effects in femtosecond laser-induced breakdown of dielectrics," *Appl. Phys. Lett.,* vol. 81, pp. 957, 2002.

[42] M. Perry, B. Stuart, P. Banks, M. Feit, V. Yanovsky and A. Rubenchik, "Ultrashort-pulse laser machining of dielectric materials," *J. Appl. Phys.,* vol. 85, pp. 6803, 1999.

[43] A. Miotello and P. M. Ossi, *Laser-Surface Interactions for New Materials Production: Tailoring Structure and Properties.* Springer Verlag, 2009.

[44] P. Lorazo, L. J. Lewis and M. Meunier, "Short-pulse laser ablation of solids: from phase explosion to fragmentation," *Phys. Rev. Lett.,* vol. 91, pp. 225502, 2003.

[45] B. Rethfeld, K. Sokolowski-Tinten, D. Von Der Linde and S. Anisimov, "Timescales in the response of materials to femtosecond laser excitation," *Appl. Phys. A,* vol. 79, pp. 767-769, 2004.

[46] L. Zhigilei, "Dynamics of the plume formation and parameters of the ejected clusters in short-pulse laser ablation," *Appl. Phys. A,* vol. 76, pp. 339-350, 2003.

[47] A. Rosenfeld, M. Lorenz, R. Stoian and D. Ashkenasi, "Ultrashort-laser-pulse damage threshold of transparent materials and the role of incubation," *Appl. Phys. A,* vol. 69, pp. 373-376, 1999.

[48] G. Petite, P. Daguzan, S. Guizard and P. Martin, "Conduction electrons in wide-bandgap oxides: a subpicosecond time-resolved optical study," *Nucl. Instrum. Methods Phys. Res. , Sect. B,* vol. 107, pp. 97-101, 1996.

[49] M. R. Kasaai, V. Kacham, F. Theberge and S. L. Chin, "The interaction of femtosecond and nanosecond laser pulses with the surface of glass," *J. Non Cryst. Solids,* vol. 319, pp. 129-135, 2003.

[50] T. Tamaki, W. Watanabe and K. Itoh, "Laser micro-welding of transparent materials by a localized heat accumulation effect using a femtosecond fiber laser at 1558 nm," *Opt. Express,* vol. 14, pp. 10460-10468, 2006.

[51] V. Koubassov, J. Laprise, F. Théberge, E. Förster, R. Sauerbrey, B. Müller, U. Glatzel and S. Chin, "Ultrafast laser-induced melting of glass," *Appl. Phys. A:Mater. Sci. Process.,* vol. 79, pp. 499-505, 2004.

[52] S. Eaton, H. Zhang, P. Herman, F. Yoshino, L. Shah, J. Bovatsek and A. Arai, "Heat accumulation effects in femtosecond laser-written waveguides with variable repetition rate," *Opt. Express.,* vol. 13, pp. 4708-4716, 2005.

[53] A. Ben-Yakar, R. L. Byer, A. Harkin, J. Ashmore, H. A. Stone, M. Shen and E. Mazur, "Morphology of femtosecond-laser-ablated borosilicate glass surfaces," *Appl. Phys. Lett.,* vol. 83, pp. 3030-3032, 2003.

[54] S. Juodkazis, H. Misawa, O. A. Louchev and K. Kitamura, "Femtosecond laser ablation of chalcogenide glass: explosive formation of nano-fibres against thermo-capillary growth of micro-spheres," *Nanotechnology,* vol. 17, pp. 4802, 2006.

[55] S. Juodkazis, H. Misawa, O. A. Louchev and K. Kitamura, "Femtosecond laser ablation of chalcogenide glass: Explosive formation of nano-fibres against thermo-capillary growth of micro-spheres," *Nanotechnology,* vol. 17, pp. 4802-4805, 2006.

[56] M. Shamim Ahsan, Y. K. Kim, M. S. Lee and M. Mahbub Hossain, "Nanostructure covered micro holes fabrication by femtosecond laser on fused silica glass surface," in *ICECE 2010 - 6th International Conference on Electrical and Computer Engineering,* 2010, pp. 384-387.

[57] B. Tan and K. Venkatakrishnan, "Synthesis of fibrous nanoparticle aggregates by femtosecond laser ablation in air," *Opt. Express.,* vol. 17, pp. 1064-1069, 2009.

[58] B. Tan, A. Dalili and K. Venkatakrishnan, "High repetition rate femtosecond laser nano-machining of thin films," *Appl. Phys. A: Mater. Sci. Process.,* vol. 95, pp. 537-545, 2009.

[59] E. Gamaly, A. Rode and B. Luther-Davies, "Ultrafast ablation with high-pulse-rate lasers. Part I: Theoretical considerations," *J. Appl. Phys.,* vol. 85, pp. 4213, 1999.

[60] A. Kiani, K. Venkatakrishnan and B. Tan, "Direct laser writing of amorphous silicon on Si-substrate induced by high repetition femtosecond pulses," *J. Appl. Phys.,* vol. 108, 2010.

[61] A. Kiani, K. Venkatakrishnan, B. Tan and V. Venkataramanan, "Maskless lithography using silicon oxide etch-stop layer induced by megahertz repetition femtosecond laser pulses," *Opt. Express.,* vol. 19, pp. 10834-10842, 2011.

[62] S. Panchatsharam, B. Tan and K. Venkatakrishnan, "Femtosecond laser-induced shockwave formation on ablated silicon surface," *J. Appl. Phys.,* vol. 105, 2009.

[63] Anonymous *Fused Silica | SiO2 Material Properties* (http://accuratus.com/fused.html ed.) *2011(8/4/2011).*

[64] K. L. Wray and T. J. Connolly, "Thermal conductivity of clear fused silica at high temperatures," *J. Appl. Phys.,* vol. 30, pp. 1702-1705, 1959.

[65] B. Luther-Davies, A. V. Rode, N. R. Madsen and E. G. Gamaly, "Picosecond high-repetition-rate pulsed laser ablation of dielectrics: The effect of energy accumulation between pulses," *Opt. Eng,* vol. 44, pp. 1-8, 2005.

[66] R. E. Russo, X. Mao, J. J. Gonzalez and S. S. Mao, "Femtosecond laser ablation ICP-MS," *J. Anal. at. Spectrom.,* vol. 17, pp. 1072-1075, 2002.

[67] A. Ben-Yakar, A. Harkin, J. Ashmore, R. L. Byer and H. A. Stone, "Thermal and fluid processes of a thin melt zone during femtosecond laser ablation of glass: The formation of rims by single laser pulses," *J. Phys. D,* vol. 40, pp. 1447-1459, 2007.

[68] M. Sivakumar, K. Venkatakrishnan and B. Tan, "Synthesis of glass nanofibers using femtosecond laser radiation under ambient condition," *Nanoscale Res. Lett.,* vol. 4, pp. 1263-1266, 2009.

[69] K. Venkatakrishnan, D. Vipparty and B. Tan, "Nanofibre fabrication by femtosecond laser ablation of silica glass," *Opt. Express.,* vol. 19, pp. 15770-15776, 2011.

[70] B. Tan and K. Venkatakrishnan, "Synthesis of fibrous nanoparticle aggregates by femtosecond laser ablation in air," *Optics Express,* vol. 17, pp. 1064-1069, 2009.

[71] R. Hergenröder, "A model for the generation of small particles in laser ablation ICP-MS," *J. Anal. at. Spectrom.,* vol. 21, pp. 1016-1026, 2006.

[72] A. Dalis and S. K. Friedlander, "Molecular dynamics simulations of the straining of nanoparticle chain aggregates: the case of copper," *Nanotechnology,* vol. 16, pp. S626, 2005.

[73] S. I. Anisimov and B. Luk'yanchuk, "Selected problems of laser ablation theory," *Physics-Uspekhi,* vol. 45, pp. 293, 2002.

[74] B. Rethfeld, V. Temnov, K. Sokolowski-Tinten, S. I. Anisimov and D. von der Linde, "Dynamics of ultrashort pulse-laser ablation: Equation-of-state considerations," in *Proceedings of SPIE,* 2002, pp. 72.

[75] M. Sivakumar, K. Venkatakrishnan and B. Tan, "Study of metallic fibrous nanoparticle aggregate produced using femtosecond laser radiation under ambient conditions," *Nanotechnology,* vol. 21, pp. 225601, 2010.

[76] C. Fan, J. Sun and J. Longtin, "Plasma absorption of femtosecond laser pulses in dielectrics," *J. Heat. Trans-T. ASME.,* vol. 124, pp. 275-283, 2002.

[77] M. Mero, J. Liu, W. Rudolph, D. Ristau and K. Starke, "Scaling laws of femtosecond laser pulse induced breakdown in oxide films," *Phys. Rev. B.,* vol. 71, pp. 115109, 2005.

[78] D. F. Farson, H. W. Choi, B. Zimmerman, J. K. Steach, J. J. Chalmers, S. V. Olesik and L. J. Lee, "Femtosecond laser micromachining of dielectric materials for biomedical applications," *J. Micromech. Microeng.,* vol. 18, pp. 035020, 2008.

[79] M. Lenzner, J. Krüger, S. Sartania, Z. Cheng, C. Spielmann, G. Mourou, W. Kautek and F. Krausz, "Femtosecond optical breakdown in dielectrics," *Phys. Rev. Lett.,* vol. 80, pp. 4076-4079, 1998.

[80] L. Zhang, J. LoU and L. Tong, "Micro/nanofiber optical sensors," *Photonic Sensors,* vol. 1, pp. 31-42, 2011.